

Development of perturbations within growing baroclinic waves

By C. SNYDER^{1*} and A. JOLY²

¹*National Center for Atmospheric Research†, USA*

²*Centre National de Recherches Météorologiques, France*

(Received 12 May 1997; revised 16 February 1998)

SUMMARY

We explore the linear stability of a growing, three-dimensional baroclinic wave by calculating the perturbation that grows most rapidly over various time intervals and at various stages in the development of the parent wave and its fronts. Three norms are used to measure growth: volume-integrated energy, enstrophy and stream function variance. The flow is assumed adiabatic and quasi-geostrophic for simplicity, and perturbations are required to have uniform potential vorticity.

These rapidly growing perturbations can produce realistic sub-structures within the parent wave, such as upper-level vorticity maxima that propagate relative to a synoptic-scale parent wave or packets of synoptic-scale waves within a planetary-wave basic state. For a synoptic-scale parent wave and the energy or enstrophy norms, however, the dominant characteristic of the fastest growing perturbations is that they rapidly evolve toward a final structure corresponding to a phase shift and slight change of shape of the original wave—in essence, the initial perturbation modifies the parent wave and the jet on which it propagates, which results in a modification, which grows in time, of the phase and amplitude of the parent wave. Amplifications in energy or enstrophy are also small compared to what would be estimated based on the locally large shears and baroclinicity within the parent wave. The fronts appear to be stabilized by the combined influences of synoptic-scale horizontal deformation and the natural movement of perturbations relative to the parent wave.

KEYWORDS: Frontal waves Growth rates Instability

1. INTRODUCTION

A variety of disturbances are observed to develop within pre-existing baroclinic waves; these disturbances include rainbands (see Houze (1993) for a survey), cyclones of various sub-synoptic scales (Browning and Roberts 1994; Blier and Wakimoto 1995; Ralph 1996), and jet streaks (Palmén and Newton 1969) or short-wave troughs. Typically, theories for the development of these disturbances are based on instabilities of steady parallel flows, which flows are assumed to model local flows within the baroclinic wave. Unfortunately, the flow in the parent wave is often neither nearly parallel on the length-scale of the instabilities, nor approximately steady on their time-scale. The stability properties of two-dimensional fronts, for example, change drastically with the addition of realistic frontogenetic flows and resulting time dependence (Joly and Thorpe 1990; Bishop and Thorpe 1994). Here, we extend previous studies of the origin of disturbances within synoptic-scale waves by considering the linear stability of a growing, three-dimensional baroclinic wave. This baroclinic wave will be referred to below as the basic state or as the parent wave.

Because of the time dependence of the parent wave, the stability analysis cannot assume a separable time dependence for the perturbations. Thus, instead of seeking modes with exponential time dependence, we calculate the perturbation that grows most rapidly over a given time interval (Lorenz 1965; Farrell 1989a; Lacarra and Talagrand 1988). Such a calculation requires a numerical model linearized about the basic state, and the adjoint or transpose of the linearized model. The resulting ‘optimal’ perturbation will depend on the beginning and length of the time interval, and on the norm chosen to measure growth. Further discussion of both the calculation and the choice of norm is given in section 3.

Our intention is to explore the phenomenology of growing perturbations within a baroclinic wave, and to expose the basic mechanisms that underlie that growth. To keep

* Corresponding author: National Center for Atmospheric Research, Mesoscale and Microscale Meteorology Division, PO Box 3000, Boulder, Colorado 80307-3000, USA.

† The National Center for Atmospheric Research is sponsored by the National Science Foundation.

the problem conceptually tractable and computationally convenient, we assume the flow to be adiabatic and quasi-geostrophic, and the perturbations to have uniform potential vorticity.

None of these assumptions is without consequence—in particular, the effects of moisture are clearly involved in determining the mesoscale structure of baroclinic waves—but frontogenesis remains inherent in the parent wave, and ensures the formation of regions of strong baroclinity and horizontal shear where perturbations may potentially grow rapidly. Thus, our calculations assess whether this potential for instability near the fronts is realized in a realistic baroclinic wave. Further discussion of the assumptions of quasi-geostrophy appears in section 2.

After presenting basic equations in section 2 and discussing the calculation of the optimal perturbations and the choice of norm in section 3, much of our attention will focus on the fastest growing disturbance in the energy norm and on parent baroclinic waves of synoptic scale (section 4). In this case, the optimal perturbation is not a frontal instability. Instead the perturbation evolves into a change in the phase and amplitude of the parent wave, and the structure of the parent wave remains qualitatively unchanged by even a finite-amplitude perturbation. Results for basic-state waves on a jet with barotropic shear or having planetary-scale appear in section 5.

We then investigate, in section 6, how the characteristics of the fastest growing disturbance depend upon the choice of norm. While the optimal perturbation in enstrophy resembles the energy optimal, the disturbance that grows fastest in stream function variance is concentrated initially at small scales, and evolves up-scale to a wave train along the upper fronts with wavelength of 2000 km. For a finite-amplitude perturbation, this wave train appears as several mobile vorticity maxima propagating downstream relative to the parent wave, much as is often seen on upper-level charts (Sanders 1988). Discussion of several aspects of the results follows in section 7: the mechanisms for the growth of the optimal perturbations, the stabilizing influence arising from the movement or propagation of perturbations relative to the parent wave, and the potential consequences of our assumption of uniform interior potential vorticity. Concluding remarks appear in section 8.

2. THE MODEL PROBLEM

Consistent with our desire for a simplified model problem, the flows considered here are adiabatic, Boussinesq and quasi-geostrophic, and are confined to a zonally (x) periodic channel that is bounded meridionally (y) by walls, and in the vertical by rigid surfaces at $z = 0, H$. The pseudo potential vorticity (hereafter PV) is also assumed to be uniform throughout the domain. None of the above assumptions can be justified rigorously, but the resulting model produces simulations that agree qualitatively and, to some extent, quantitatively with observed baroclinic waves (e.g. Rotunno and Bao 1996).

Nondimensionalizing vertical distance by H , horizontal distance by the Rossby radius NH/f , velocities by U , time by NH/fU , and ϕ , the geostrophic stream function, by NHU , where f is the Coriolis parameter and N the rest-state buoyancy frequency, the flow is governed by

$$\phi_{xx} + \phi_{yy} + \phi_{zz} = 0, \quad (1a)$$

with

$$(\partial_t + u\partial_x + v\partial_y)\phi_z = 0 \quad \text{at } z = 0, 1. \quad (1b)$$

Here f and N are taken to be constants, the channel width is y_B , the along-channel periodicity is x_B , $(u, v) = (-\phi_y, \phi_x)$ defines the geostrophic velocity, and $\theta = \phi_z$ defines the deviation of potential temperature due to the motion. (See Pedlosky (1987) for a

derivation of the quasi-geostrophic equations.) At the channel walls the normal flow is zero, and the zonal-mean zonal velocity is independent of time:

$$\phi_x = \int_0^{x_B} \phi_{yt} \, dx = 0 \quad \text{at } y = 0, y_B$$

Where dimensional values are used, they will be based on $U = 29.5 \text{ m s}^{-1}$, $N = 1.13 \times 10^{-2} \text{ s}^{-1}$, $H = 9 \text{ km}$ and $f = 10^{-4} \text{ s}^{-1}$.

Relative to quasi-geostrophy, semi-geostrophic dynamics would more accurately describe the frontogenesis that occurs within baroclinic waves (Hoskins and West 1979; McWilliams and Gent 1980), a possibly important distinction since one expects that rapidly growing disturbances may often be localized along fronts. The quasi-geostrophic set, however, has computational advantages, since familiar norms, such as total energy, are nearly diagonal. Furthermore, scaling indicates that semi-geostrophy and quasi-geostrophy describe disturbances to fronts (i.e. along-front variations) with the same accuracy (Snyder 1995). For instabilities of a barotropic shear layer, comparisons of semi-geostrophic and quasi-geostrophic solutions support this conclusion (Malardel *et al.* 1997).

The assumption of uniform interior PV also needs careful examination and is discussed further in section 7, together with its possible effects on our results.

Before considering the development of perturbations, we require a parent baroclinic wave that is a nonlinear time-dependent solution to (1). This basic state is calculated as follows: we begin with a zonal jet $U(y, z)$ and associated potential temperature $\Theta(y, z)$, where $U_z = -\Theta_y$. Exact specifications are given below for various cases. The zonal jet is then perturbed with small-amplitude noise, from which the most unstable mode with wavelength x_B emerges. This mode is scaled to a specified amplitude and added to the original zonal jet to form initial conditions for an integration of (1).

The resulting solution, denoted by an overbar and consisting of the growing baroclinic wave superposed on the zonal jet, is the basic state about which we will calculate the growth of perturbations. Perturbations that are sufficiently small evolve according to the linearization of (1), namely,

$$\phi'_{xx} + \phi'_{yy} + \phi'_{zz} = 0, \tag{2a}$$

$$(\partial_t + \bar{u}\partial_x + \bar{v}\partial_y)\phi'_z + (u'\partial_x + v'\partial_y)\bar{\theta} = 0 \quad \text{at } z = 0, 1, \tag{2b}$$

where primes denote perturbations.

3. CALCULATION OF THE OPTIMAL PERTURBATION

(a) Basic techniques

To fix notation, we next outline the techniques used in the calculation of the optimal perturbations. More complete discussions appear elsewhere (Lacarra and Talagrand 1988; Buizza *et al.* 1993; Moore and Farrell 1993).

Both (1) and (2) are solved using a semi-spectral method (Joly 1995, appendix) based on an expansion of the form:

$$\phi = \sum_{n=-N}^N \sum_{m=1}^{M(n)} (A_{nm}e^{-\kappa_{nm}z} + B_{nm}e^{\kappa_{nm}z}) \sin(m\pi y/y_B) \exp(2in\pi x/x_B), \tag{3}$$

where $\kappa^2 = k^2 + l^2$. The truncation is elliptic, with $M(n) = \lfloor M(0)(1 + n^2/N^2)^{1/2} \rfloor$.

The numerical solutions for the basic state and the perturbations can be considered as real vectors $\bar{\phi}(t)$ and $\phi'(t)$, whose components include both the real and imaginary parts of the spectral coefficients. By definition, ϕ' satisfies the linear equation

$$\phi'_f = \mathbf{L}\phi'_0, \tag{4}$$

where $\phi'_0 = \phi'(t_0)$ and $\phi'_f = \phi'(t_f)$. The matrix \mathbf{L} depends on the initial time t_0 , the final time t_f , and the basic state $\bar{\phi}$.

In order to calculate the perturbation that grows most from t_0 to t_f , we define a norm to measure ϕ' . The norm $\langle \phi \rangle^2$ will be based on the scalar product

$$\langle \phi, \psi \rangle = \phi^T \mathbf{S} \psi,$$

where the superscript T indicates a transpose and \mathbf{S} is a symmetric, positive definite matrix.

The optimal perturbation maximizes $\nu^2 = \langle \phi'_f \rangle^2 / \langle \phi'_0 \rangle^2$. Using (4) and the fact that \mathbf{S} is symmetric,

$$\begin{aligned} \langle \phi'_f, \phi'_f \rangle &= \phi_0^{T'} \mathbf{L}^T \mathbf{S} \mathbf{L} \phi'_0 \\ &= \langle \phi'_0, \mathbf{K} \phi'_0 \rangle, \end{aligned}$$

where $\mathbf{K} = \mathbf{S}^{-1} \mathbf{L}^T \mathbf{S} \mathbf{L}$; it is then straightforward to show that ν is maximized by the leading eigenvector of \mathbf{K} . Thus, the optimal perturbation is that leading eigenvector, and has amplification ν that is the square root of the leading eigenvalue of \mathbf{K} .

More generally, one can define different norms to be used at the initial and final times. Denoting these initial and final norms by the subscripts 0 and f, respectively, the optimal perturbation then maximizes $\nu^2 = \langle \phi'_f \rangle_f^2 / \langle \phi'_0 \rangle_0^2$, and is the leading eigenvector of $\mathbf{K} = \mathbf{S}_0^{-1} \mathbf{L}^T \mathbf{S}_f \mathbf{L}$.

Both \mathbf{L} and \mathbf{L}^T are known implicitly. The effect of \mathbf{L} on a perturbation ϕ'_0 may be obtained by numerical integration of (2) from t_0 to t_f . The effect of \mathbf{L}^T may be computed given the transpose (or adjoint) of the linearized numerical model.

We calculate the optimal perturbation by the power method, that is, by repeatedly applying \mathbf{K} to a vector until the result converges to the leading eigenvector. Although other eigenvectors of \mathbf{K} may have eigenvalues larger than 1 and represent amplifying perturbations, only the optimal perturbation will be considered here.

(b) *Choice of norm*

The optimal perturbation typically depends on the norm (Farrell 1989a; Vukicevic 1993; Joly 1995); thus, the choice of norm merits careful consideration.

We seek a norm that identifies disturbances that will emerge from (and come to dominate) initial noise, analogous to the exponentially growing, most unstable mode on a steady basic state. But, because we consider growth over a finite time interval, and because that interval is comparable to the time-scales expected for growth of disturbances, the perturbations retain memory of their initial conditions. Thus, the preferred norm should explicitly account for statistics of initial noise from which perturbations are thought to arise.

This idea is familiar in the context of the growth of forecast errors, where the 'initial noise' is simply composed of errors in the analysis used as initial conditions for the forecast (Houtekamer 1995; Ehrendorfer and Tribbia 1996). The statistics of the initial conditions can be accounted for formally through the use of the covariance matrix \mathbf{C} given by

$$\mathbf{C} = [\phi'_0 \phi_0^{T'}],$$

where square brackets denote the expectation operator or, equivalently, an average over a large ensemble of realizations of the initial analysis for a given observational network and data-assimilation scheme; ϕ'_0 now represents deviations from the ensemble-mean analysis. Setting $\mathbf{S}_0 = \mathbf{C}^{-1}$, the initial norm then gives large weights to unlikely initial conditions. If, for example, the components of ϕ'_0 are uncorrelated, \mathbf{C} is a diagonal matrix consisting of the variances and the norm based on \mathbf{C}^{-1} gives largest weight to the component of ϕ'_0 with smallest variance.

Still, it is not obvious that we have made progress. What indeed are the statistics appropriate to the initial noise to be superposed on the basic-state baroclinic wave? The fundamental problem (both conceptual and practical) is to distinguish between the basic state and the perturbations. One approach would be to filter planetary waves and baroclinic waves (along with their attendant fronts) from observational data; the remaining small-scale motions would be the 'noise'. Yet this is exceedingly difficult to do in practice because of the broad spectral signature of fronts. Alternatively, one might seek structures of sub-synoptic scale that, because of their longevity, would dominate the statistics of the noise. Such structures may exist (Sanders 1988; Lefevre and Nielsen-Gammon 1995) and be identified as 'short waves'.

Yet another approach, as proposed by Palmer *et al.* (1998), is to consider the atmosphere as a dynamical system and base the norm on the local structure of the attractor. They suggest that the volume-integrated perturbation enstrophy may capture the important properties of such a norm.

In our view the choice of norm remains an open question. Rather than attempting to account for the statistics of the initial conditions, most results presented here will employ total energy as norm, which in its continuous form is

$$\langle \phi' \rangle^2 = \int dV (\phi_x'^2 + \phi_y'^2 + \phi_z'^2).$$

Optimal modes for two other norms, volume-integrated stream function variance ϕ'^2 and enstrophy $(\phi'_{xx} + \phi'_{yy})^2$, are discussed in section 6. Matrices \mathbf{S} appropriate to the discrete form of each norm can be found in Joly (1995).

4. ENERGY-OPTIMAL PERTURBATIONS ON THE HOSKINS–WEST WAVE

We first consider as a basic state a baroclinic wave from Hoskins and West (1979; HW hereafter) and employ the energy norm. This section concentrates mainly on the phenomenology of the optimal perturbation on the HW wave; discussion of the dynamics follows in section 7.

(a) *The parent baroclinic wave*

The parent baroclinic wave grows on a zonal jet shown in Fig. 1 of HW and given by their Eq. (17) with $\mu = 1$. The domain has dimensions $x_B = 4.0$ and $y_B = 5.5$, corresponding to dimensional values of 4090 km and 5600 km, respectively, and the numerical solution (for both the basic state and perturbations) truncates (3) at $N = 15$ and $M(0) = 42$. The basic-state integration is initialized with the most unstable mode normalized so that $\max(\bar{v})$ has a dimensional value of 1.7 m s^{-1} . This mode grows at 0.5 d^{-1} and propagates with phase speed 12 m s^{-1} .

The parent wave, displayed in Fig. 1 at day 4 and day 6 of its development, exhibits structure generally familiar from synoptic charts and from other idealized studies of baroclinic waves. By day 6 of the integration, the wave in $\bar{\theta}$ has begun to break, and regions of

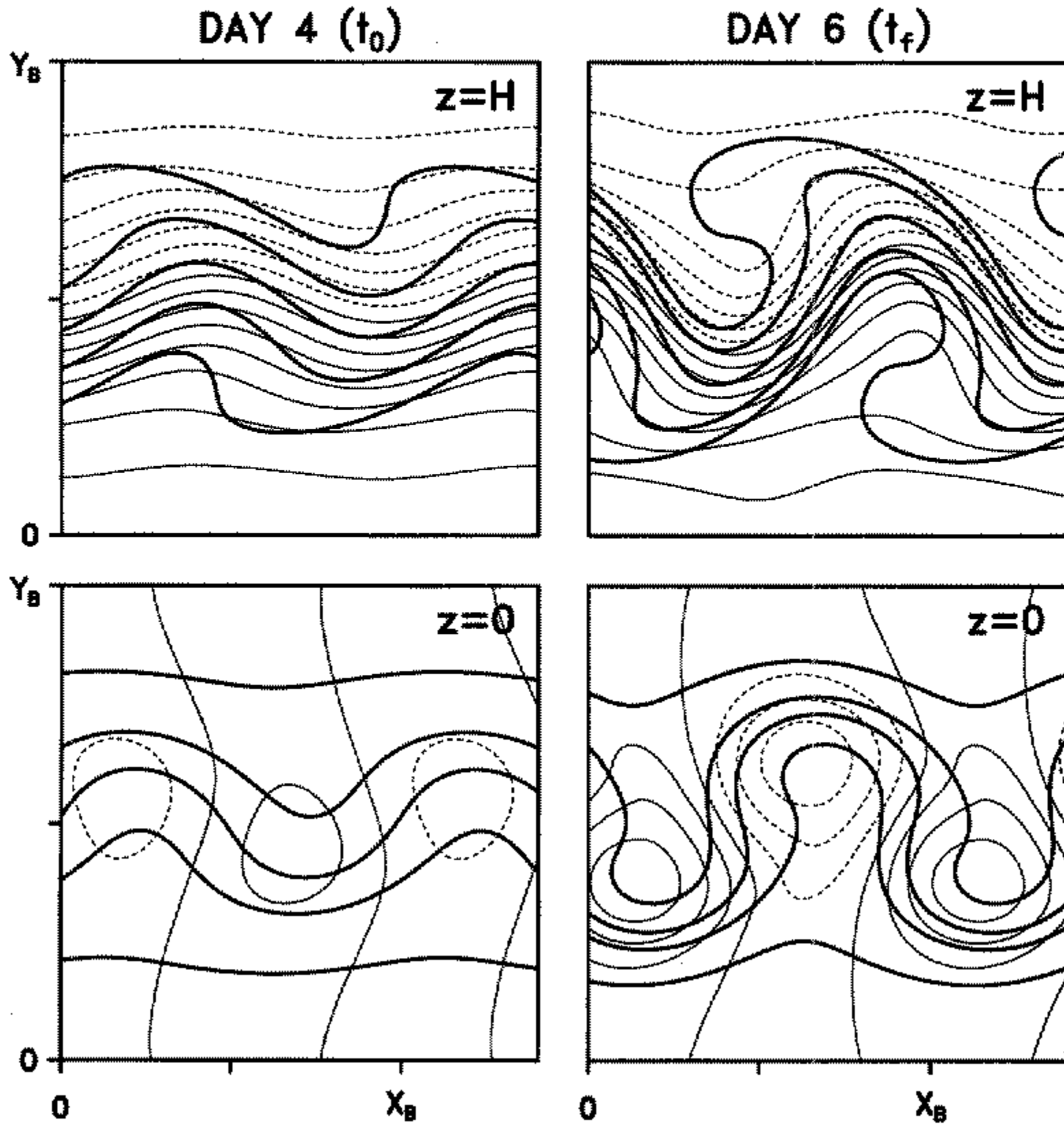


Figure 1. The basic-state baroclinic wave at day 4 (left panels) and day 6 (right panels). Contours of potential temperature ($\bar{\theta}$; heavy solid lines) and geostrophic stream function ($\bar{\phi}$; thin lines, negative values dashed) are shown at the surface ($z = 0$, lower panels) and the lid ($z = H$, upper panels), with contour intervals of 6 K and $200 \text{ m}^2 \text{ s}^{-2}$ for $\bar{\theta}$ and $\bar{\phi}$, respectively. The domain shown spans 1.4 wavelengths of the basic state.

strong gradients (the quasi-geostrophic version of fronts) have formed at both the surface and the lid.

For future reference, note the flow symmetries

$$\bar{\phi}(x, y) = -\bar{\phi}(x + x_B/2, y_B - y), \quad \bar{\theta}(x, y) = -\bar{\theta}(x + x_B/2, y_B - y), \quad (5)$$

where the area averages of $\bar{\phi}$ and $\bar{\theta}$ are taken to be zero without loss of generality.

(b) *The optimal perturbation for $t_0 = 4 \text{ d}$, $t_f = 6 \text{ d}$*

A typical time-scale for the development of observed disturbances within baroclinic waves is 24–48 h, although development may be more rapid than this for disturbances of sufficiently small scale. Thus, we choose a time interval $t_f - t_0 = 48 \text{ h}$ for the calculation of the optimal perturbation. We also take $t_0 = 4 \text{ d}$, as we are interested in a parent wave of significant amplitude. Other initial times, and other time intervals, are discussed below.

Over the chosen time interval, the optimal perturbation amplifies by a factor of $\nu = 5.0$ (that is, its energy increases by a factor of $\nu^2 = 25$). In contrast, Ehrendorfer and Errico (1995) find an amplification of 5.5 over just 24 h for the optimal perturbation growing on an observed, rapidly deepening cyclone, and Buizza and Palmer's (1995) year-long climatology of singular vectors indicates that maximum amplifications are typically 8 in

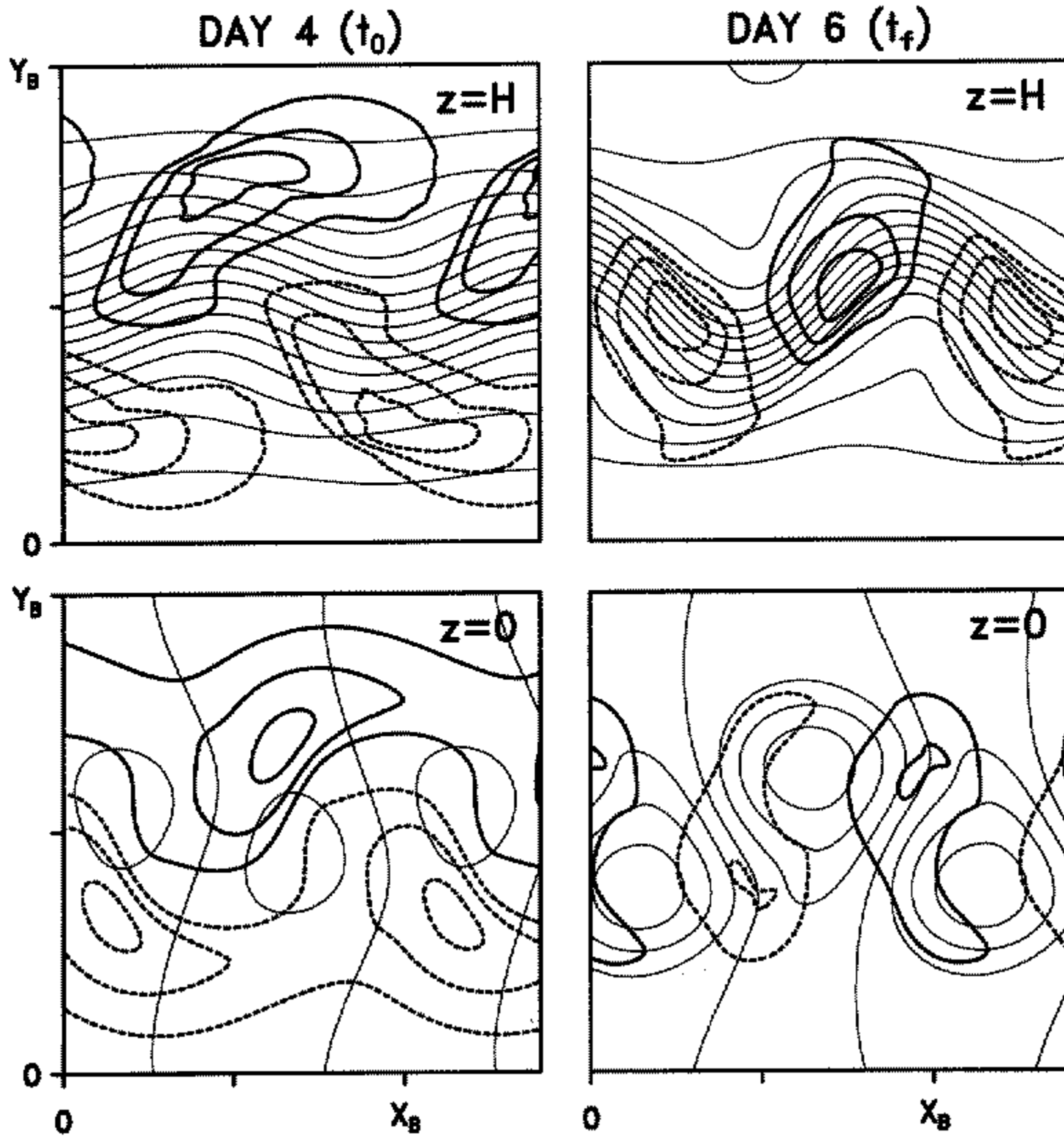


Figure 2. The optimal perturbation for initial time $t_0 = 4$ d and final time $t_f = 6$ d: perturbation geostrophic stream function (ϕ' ; thick lines, negative values dashed) at $t = t_0$ (left panels) and $t = t_f$ (right panels); and at the surface ($z = 0$, lower panels) and the lid ($z = H$, upper panels). Contours at t_0 are plotted at 1/4, 1/2 and 3/4 of the maximum ϕ' at the lid; at t_f , contour levels are increased by a factor of 6. For reference, the basic-state geostrophic stream function is shown as in Fig. 1 (but solid lines are used for both positive and negative values).

36 h. Our use of a climatological jet speed $U = 30 \text{ m s}^{-1}$ explains some of this difference, as doubling the jet speed (arguably closer to that of the observed jet in Ehrendorfer and Errico) would halve the time-scale, and the amplification of 5.0 would then apply to a 24 h interval. Reduction of the optimal amplification produced by assuming uniform interior PV is discussed further in section 7(c).

Figure 2 shows ϕ' and $\bar{\phi}$ at the surface and the lid, and at the initial and final times—note that the contour values increase by a factor of 6 from t_0 to t_f . The optimal perturbation shares the symmetry of (5), although the numerical calculations do not enforce it.

At the initial time the optimal perturbation has largest amplitude at the edges of the jet in the basic-state flow, and is elongated from the centre of the channel outward and westward. The perturbation also has a significant zonal mean component at t_0 . Two days later the perturbation is less elongated (particularly at the lid), has a relatively small zonal mean, and to a first approximation lies one quarter wavelength out of phase from the parent wave. Throughout the development of the perturbation, ϕ' maintains a westward phase tilt with height.

The potential-temperature perturbation ($\theta' = \phi'_z$) emphasizes smaller scales than ϕ' . As shown in Fig. 3, the small scales are most evident aloft at t_0 , but by $t = t_f$ fine structure in θ' appears at both the surface and the lid. There is a strong tendency by the final time

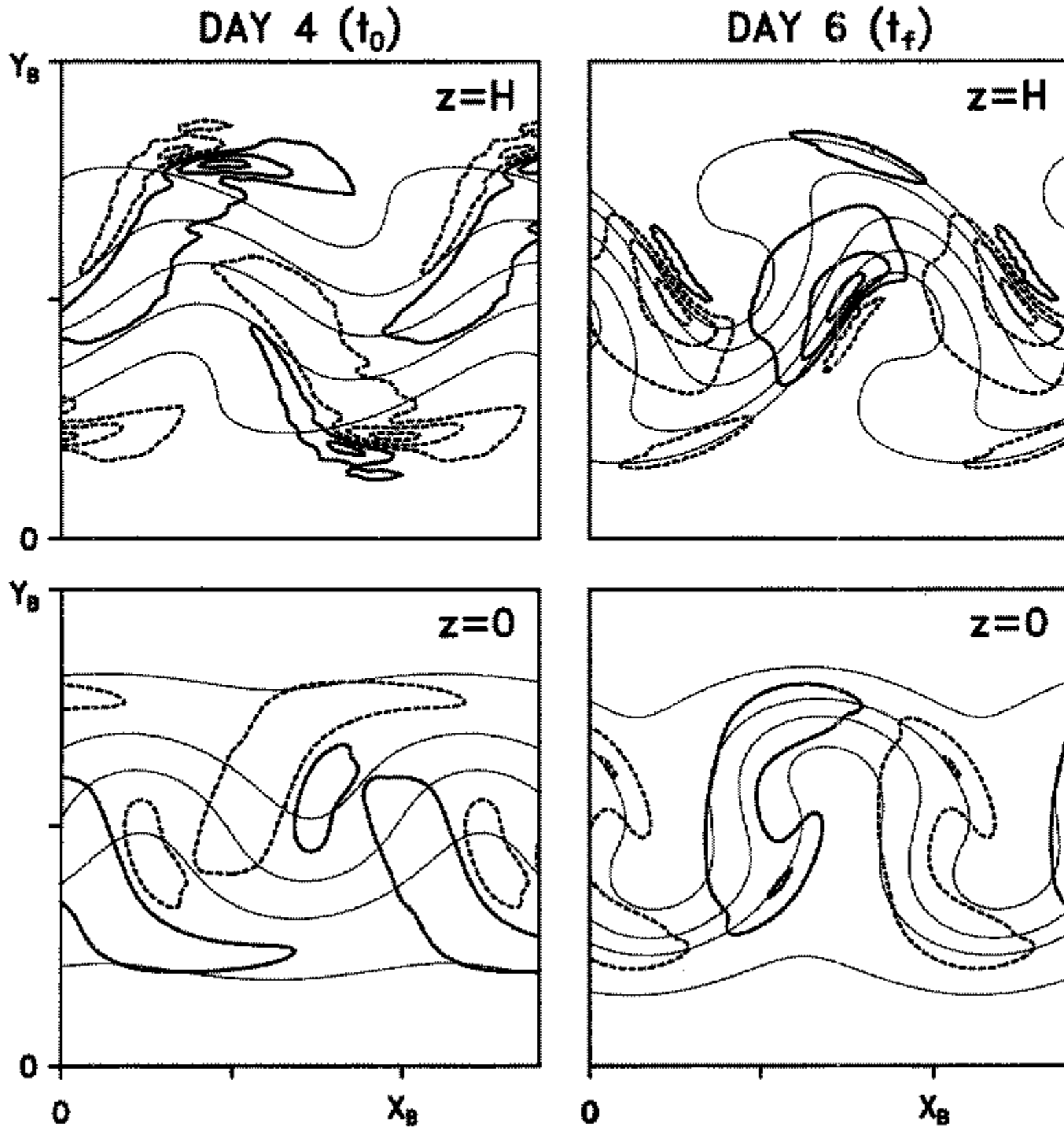


Figure 3. As Fig. 2, except showing perturbation and basic-state potential temperature (θ' and $\bar{\theta}$, respectively); contours of θ' at initial time t_0 are plotted at $1/6$, $1/2$ and $9/10$ of the maximum θ' at the upper lid, and contour levels at final time t_f are increased by a factor of 5.

for the maxima in θ' , and the fine structure, to be concentrated along the largest gradients in $\bar{\theta}$.

Because the flow dynamics are governed by conservation of θ at the upper and lower boundaries, perturbations naturally tend to localize where gradients of $\bar{\theta}$ are large. (Where $|\nabla\bar{\theta}|$ is large, there will typically be a large source for θ' in (2b); where $|\nabla\bar{\theta}|$ is small and this source is weak, θ' will eventually evolve toward the smallest resolved scale through shearing by the basic-state flow.) The 'streaky' structure in θ' at $t = t_f$ will thus be characteristic of perturbations to any basic state with localized gradients in $\bar{\theta}$ (or, more generally, in PV). For example, if the basic-state flow possessed a jump in $\bar{\theta}$, perturbations would have a δ -function in θ' along that jump.

Given the rapid growth of the optimal perturbation and the small scales present in θ' , it is important to consider the limits of the assumed linearity of the perturbation dynamics (2b). Figure 4 presents the variation of the amplification ν with the initial amplitude of the perturbation, for convenience measured by the maximum of $|\theta'|$ at the surface. Linear dynamics appears a reasonable approximation up to $\max |\theta'| = 1$ K, since the amplification is then nearly independent of amplitude, while beyond that threshold amplifications steadily decrease. In the remainder of this subsection, we will assume a perturbation with $\max |\theta'(z = 0, t = t_0)| = 1.5$ K—at that amplitude the perturbation results in notable changes when added to the parent wave, yet our linearized calculation of the optimal remains useful.

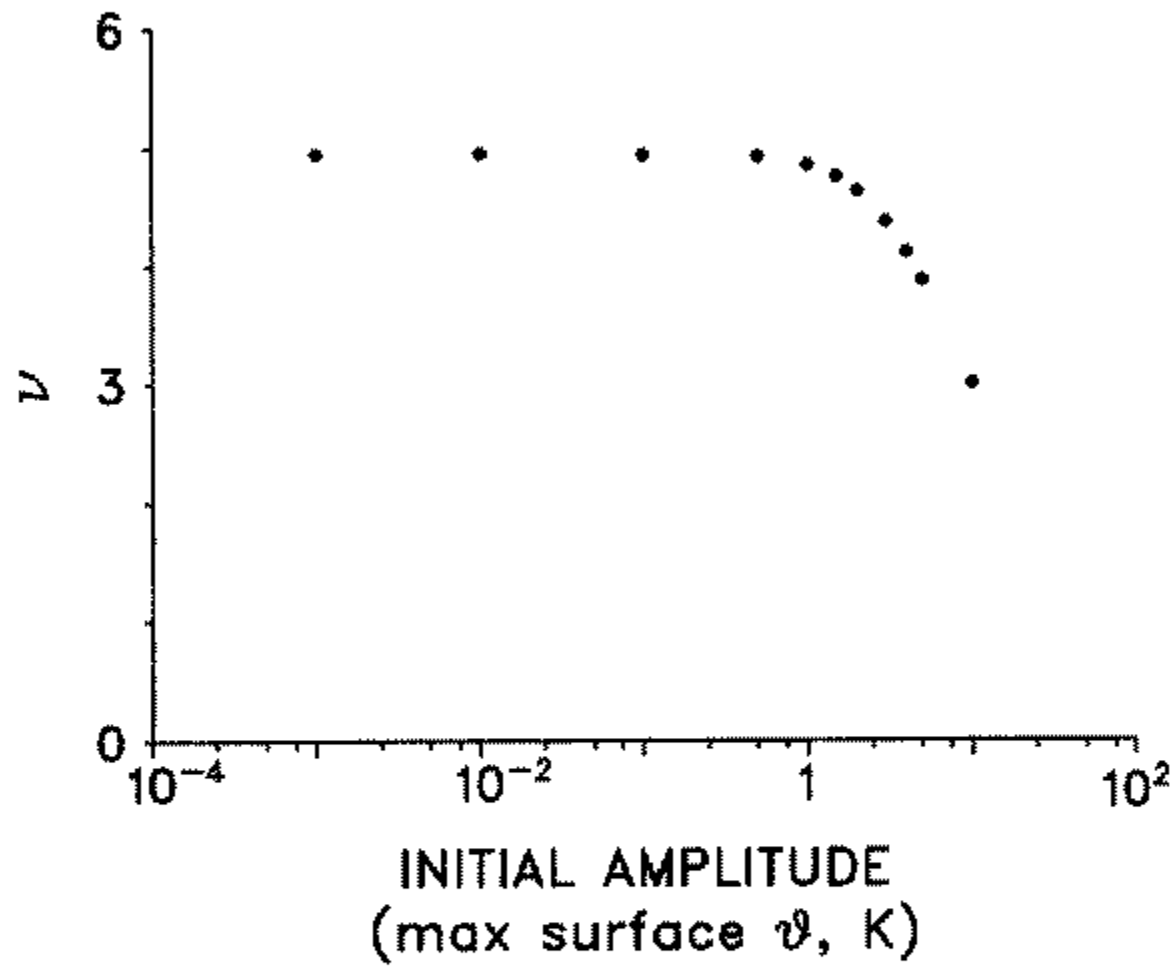


Figure 4. Amplification ν (in energy) for the perturbation shown in Figs. 1 and 2 as a function of initial amplitude (measured by the maximum of perturbation potential temperature at the surface).

The time evolution of θ' at the lid is shown in Fig. 5. Unlike previous figures, contour levels do not vary between panels in order to emphasize the growth of θ' . In the first period of 0.4 d and near its maximum, θ' is locally nearly conserved and the time dependence of θ' arises mainly through advection of the perturbation by the basic state, i.e. through the term $(\bar{u}\partial_x + \bar{v}\partial_y)\phi'_z$ in (2b). Much as in Farrell (1989b), these advectons act to compress the initially elongated strip of θ' . Elsewhere and subsequently, the development of θ' is equally characteristic of wave propagation: θ' is not conserved and the term $(u'\partial_x + v'\partial_y)\bar{\theta}$ is important in (2b), indicating that the perturbation is interacting with gradients of $\bar{\theta}$ as well as being advected by (\bar{u}, \bar{v}) . Similar observations apply to the evolution of θ' at the surface (not shown).

Although the maximum $|\theta'|$ amplifies by a factor of more than 5, the obviousness of 'wiggles' in θ contours diminishes with time. This is caused by two factors mentioned previously. First, θ' becomes increasingly colocated with large $|\nabla\bar{\theta}|$, thereby producing displacements of θ contours that grow little, or decay, with time. Second, the perturbation becomes increasingly similar in scale to the parent wave, so that the presence of the perturbation results mainly in a change in the phase and overall shape of the θ contours; perturbations of the sign shown in Fig. 5 retard the phase and elongate ridges and troughs of the parent wave.

Effects of nonlinearity may be seen by comparing the top right panel of Fig. 3 with the bottom right of Fig. 5. For the finite-amplitude perturbation, the maximum θ' broadens and shifts in the direction normal to the θ contours, and gradients of θ' weaken, all of which are consistent with a finite-amplitude displacement of contours of $\theta = \bar{\theta} + \theta'$.

(c) Other t_0 and time intervals

Even for a steady basic state, the amplification and structure of the optimal perturbation depend on $t_f - t_0$. For an evolving basic state, one expects dependence on t_0 as well as $t_f - t_0$, at least as t_0 varies over the time-scale of the basic-state evolution. Here, the basic state develops from an almost straight jet at day 0 to a large-amplitude baroclinic wave by day 6.

Consider first how the optimal amplification varies with t_0 for fixed $t_f - t_0 = 2$ d. Figure 6(a) shows both the optimal amplification and the amplification of the parent wave

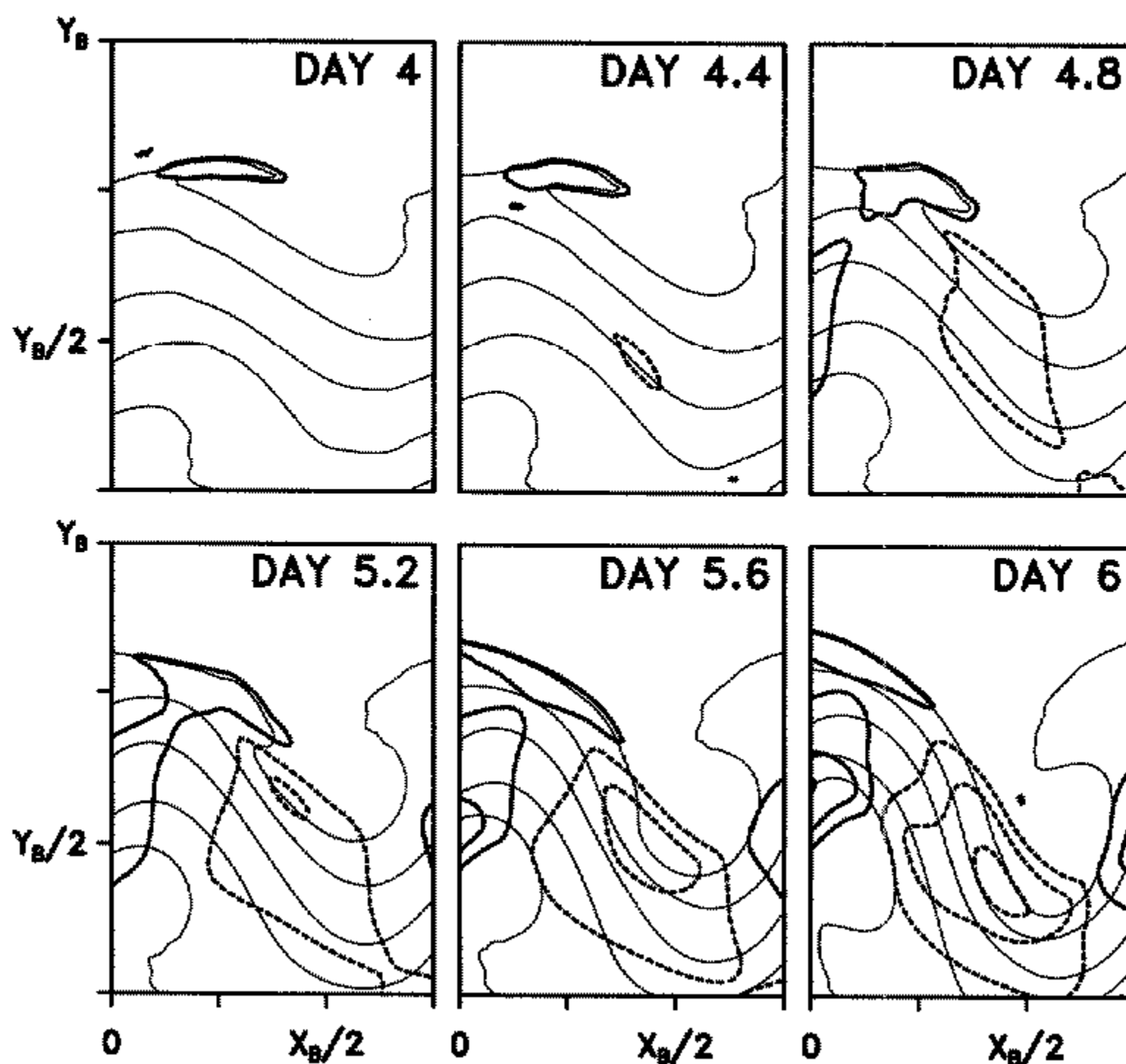


Figure 5. Time evolution of the optimal perturbation (initial time $t_0 = 4$ d, final time $t_f = 6$ d) at finite amplitude. Contours of potential temperature for the perturbation (θ' ; thick lines, at 3 K, 9 K 18 K) and basic-state plus perturbation ($\theta = \bar{\theta} + \theta'$; thin lines) at the upper lid are shown every 0.4 d between $t = t_0, t_f$. Note that the domain shown comprises only 3/4 of a wavelength of the parent wave and only the northern 3/4 of the channel width, and moves at the phase speed of the parent wave (12 m s^{-1}). The initial perturbation has $\max \theta' = 1.5 \text{ K}$ at the surface $z = 0$.

as functions of t_0 , where the amplitude of the parent wave is measured by the total energy of deviations from the original zonal jet, and the amplification is the square root of the ratio of the energies at t_0 and t_f . Initially, both the parent wave and the optimal perturbation grow at a similar rate. The optimal amplification, however, increases with t_0 , while the growth of the parent wave decreases as its nonlinear equilibration begins. By $t_0 = 6$ d, amplification of the optimal is nearly 5 times that of the parent wave.

The variation of the optimal amplification with $t_f - t_0$ is displayed in Fig. 6(b), using $t_0 = 2$ d. As expected, the amplification increases steadily with $t_f - t_0$.

The initial structure of the optimal also varies significantly with t_0 . The initial θ' at the lid is shown in Fig. 7 for $t_0 = 2$ d and 6 d; results for $t_0 = 4$ d appear in the upper left panel of Fig. 3. While there are similarities among the optimals, such as the tendency for elongated maxima and a change in the orientation of the pattern at the edge of the jet, θ' systematically contracts into elongated ribbons as t_0 increases and the parent wave grows, and those ribbons increasingly align with $\bar{\theta}$ contours (and thus the basic-state flow) in the centre of the jet. When $t_0 = 6$ d, the ribbons are near the limits of the resolution of the numerical computation, but the structure and amplification are little changed by a doubling of the resolution. Behaviour at the surface (not shown) is broadly similar, with θ' elongating into ribbons by $t_0 = 6$ d.

The evolved structure of the perturbation (not shown) varies relatively less than the initial structure and retains certain characteristics for all t_0 and $t_f - t_0$ examined. Specif-

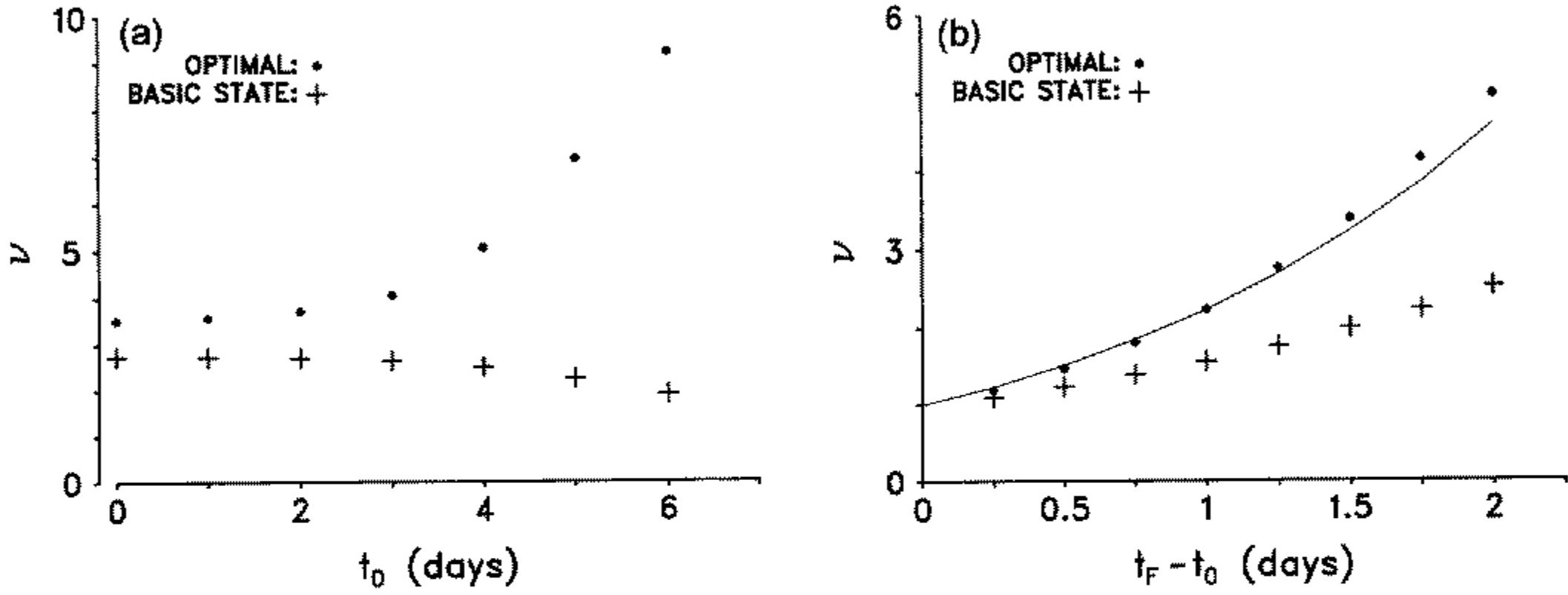


Figure 6. Optimal amplification ν as a function of: (a) t_0 for fixed $t_f - t_0 = 2$ d, where t_0 and t_f are the initial and final times, respectively, and (b) $t_f - t_0$ for fixed $t_0 = 4$ d. Amplification of the parent wave in the basic state is also shown (crosses; see text for definition of amplification). The thin solid line in (b) indicates the amplification predicted (see (6)) by $\nu(t) = \alpha t a(t)$, where $a(t)$ denotes the amplitude of the parent wave and α is chosen to reproduce the optimal amplification at $t_f - t_0 = 1$ d.

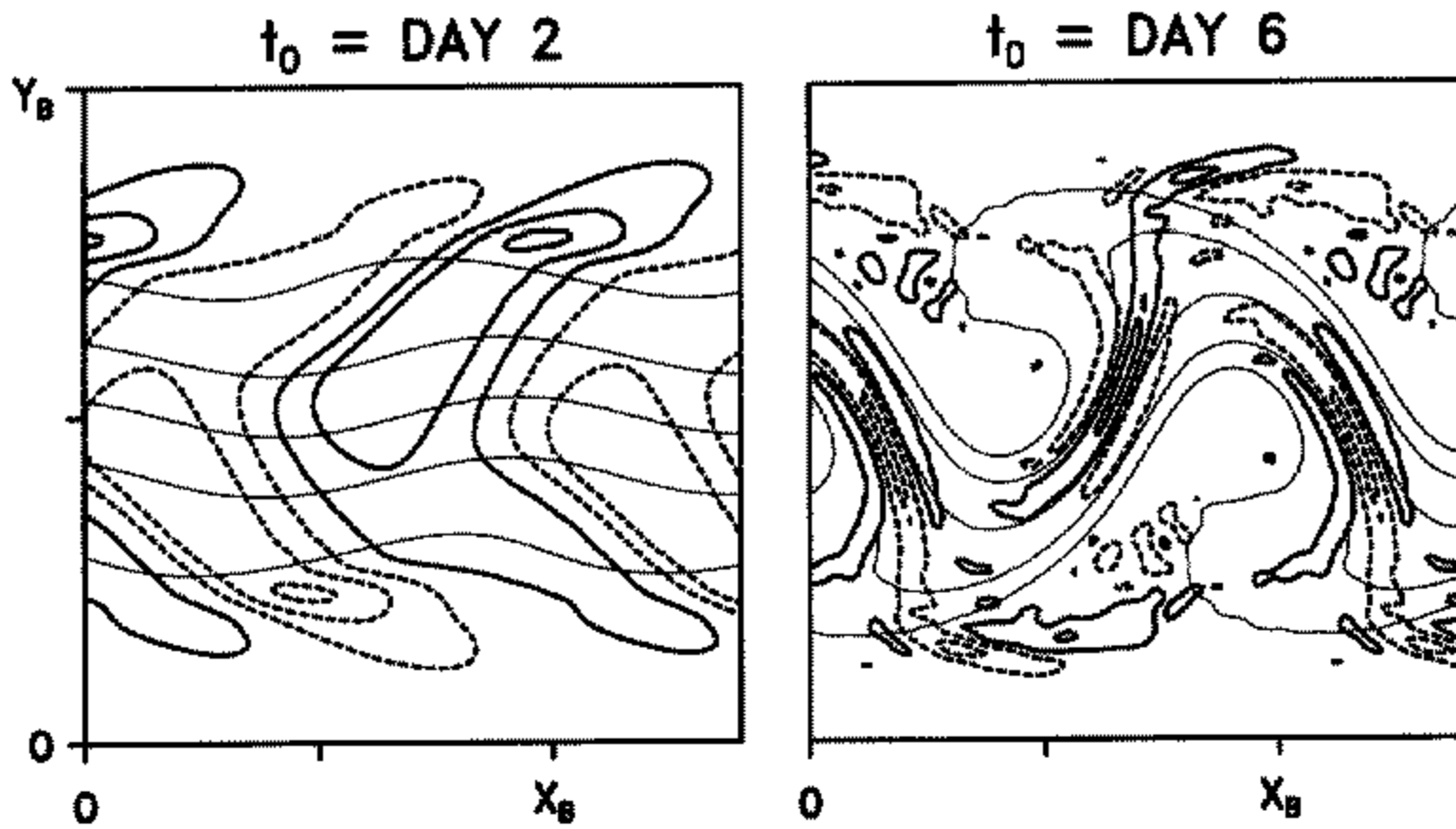


Figure 7. Optimal perturbations at $t = t_0$ for $t_f - t_0 = 2$ d and $t_0 = 2$ d (left panel) and $t_0 = 6$ d (right panel). Contours of θ' (thick lines) at $z = H$ are plotted at $1/6$, $1/2$ and $9/10$ (left panel), and $1/4$ and $3/4$ (right panel) of the maximum θ' . Contours of $\bar{\theta}$ (thin lines) are shown as in Fig. 3 for reference. See text for definitions of variables.

ically, the perturbation at final time typically has scale comparable to that of the parent wave from which it is approximately one-quarter wavelength out of phase. This behaviour is not surprising when $t_0 \leq 2$ d: since the parent wave has small amplitude, the optimal perturbation is almost the same as for the original jet, and its evolved structure tends to resemble the most unstable normal mode on that jet, that is, it resembles the parent wave. For t_0 as large as 4 d, however, the parent wave has sufficient amplitude to alter the optimal perturbation's initial structure and amplification, as evidenced by Figs. 6(a) and 7. A mechanism that explains the evolved structure of the optimal in this case is proposed in section 7(a).

In contrast to the situation at $t = t_0$, the evolved structure of the perturbation (not shown) has little qualitative dependence on either t_0 or $t_f - t_0$. At the final time, the perturbation typically has grown in scale to be comparable with that of the parent wave from

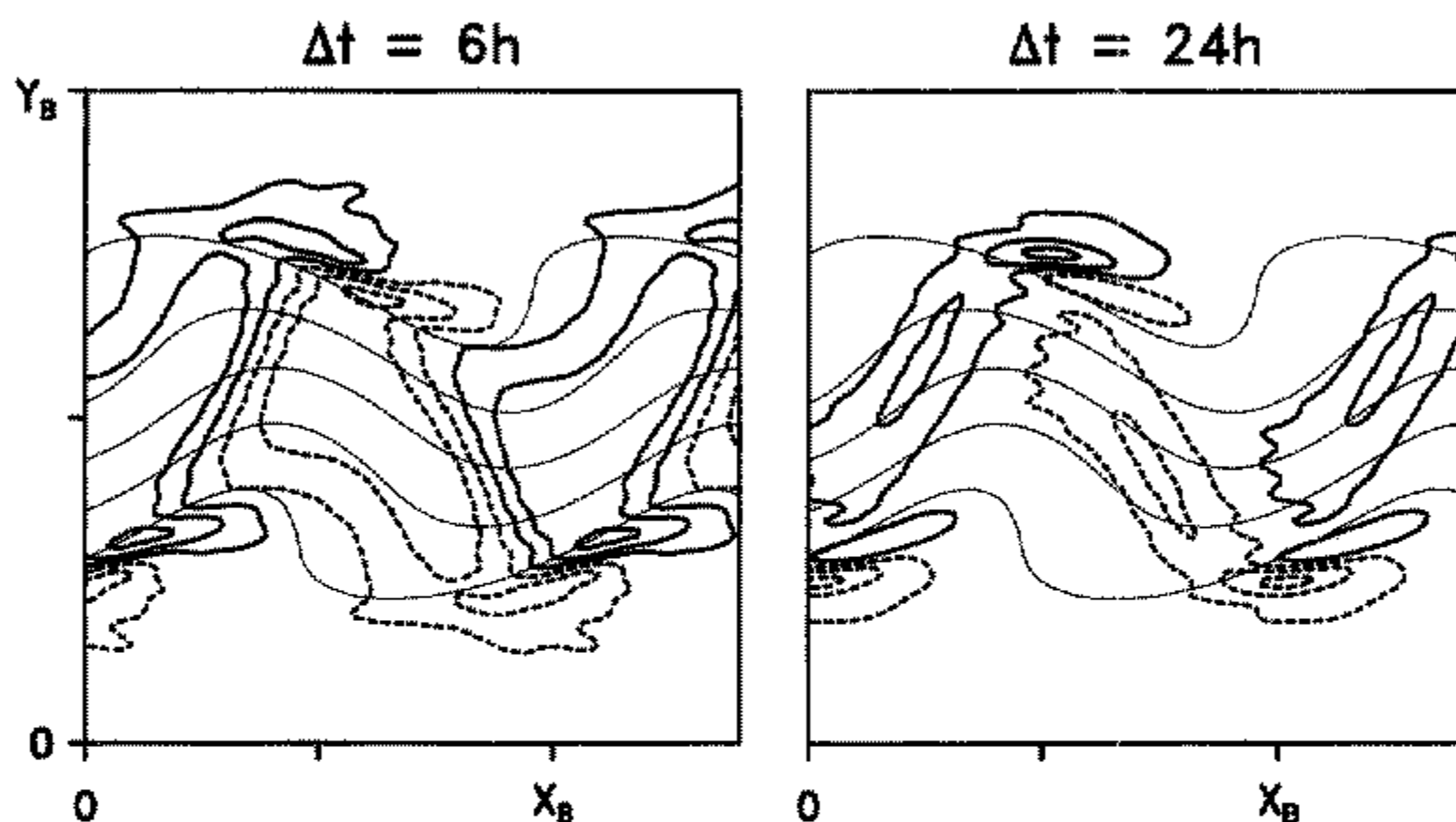


Figure 8. Optimal perturbations at $t = t_0 = 4$ d for $t_f - t_0 = 6$ h (left panel) and $t_f - t_0 = 24$ h (right panel). Contours of θ' (thick lines) at $z = H$ are plotted at $1/6$, $1/2$ and $9/10$ of the maximum θ' , and contours of $\bar{\theta}$ (thin lines) are shown as in Fig. 3 for reference. See text for definitions of variables.

which it is approximately one-quarter wavelength out of phase. There is a tendency as t_0 increases for θ' to become concentrated along the basic-state fronts, but this has little effect on the coarse-grained structure of the optimal, such as that of ϕ' .

The optimal structure is noticeably less dependent on $t_f - t_0$ than on t_0 . As shown by Fig. 8 and the upper left panel of Fig. 3, θ' is qualitatively similar for $t_f - t_0 = 0.25$ d, 1 d and 2 d, although the tendency for θ' to elongate into ribbons as the time interval lengthens is evident (similar to that for increasing t_0).

5. OTHER BASIC STATES

(a) Basic state with barotropic shear

Observed baroclinic waves do not typically possess the symmetry of (5). To explore the importance of an asymmetric parent wave, we have repeated the calculation of section 4 with a constant barotropic shear $\bar{u}_s = \Lambda y$ added to the HW jet, where $\Lambda = -0.03 f$ (or -0.1 in nondimensional units). With the addition of \bar{u}_s , the basic state no longer satisfies (5). Instead, the unstable mode tends to tilt with the barotropic shear, and the finite-amplitude wave exhibits a distinctive 'wrapping' of $\bar{\theta}$ contours around lows for cyclonic shear ($\Lambda < 0$; Davies *et al.* (1991) show an example).

Asymmetries relative to (5) are obvious in the energy-optimal perturbation (not shown) once the basic-state wave reaches finite amplitude. In particular, the perturbation at $t = t_0$ is now localized at the entrance to the region of strongest upper-level frontogenesis, upstream of the trough of the parent wave and on the cyclonic-shear side of the jet. Asymmetries persist in the evolved structure of the optimal, but they are much reduced. Overall, the perturbation at $t = t_f$ resembles that for the symmetric jet and basic state: the perturbation has grown in scale, with significant amplitude at the wavelength of the parent wave, from which it is one-quarter wavelength out of phase.

(b) Long-wave basic state

The calculations of the previous sections were motivated by observations of smaller-scale structure within synoptic-scale baroclinic waves. Yet synoptic-scale baroclinic waves often grow in an environment modulated by planetary waves, motivating the consideration here of a planetary-scale parent wave.

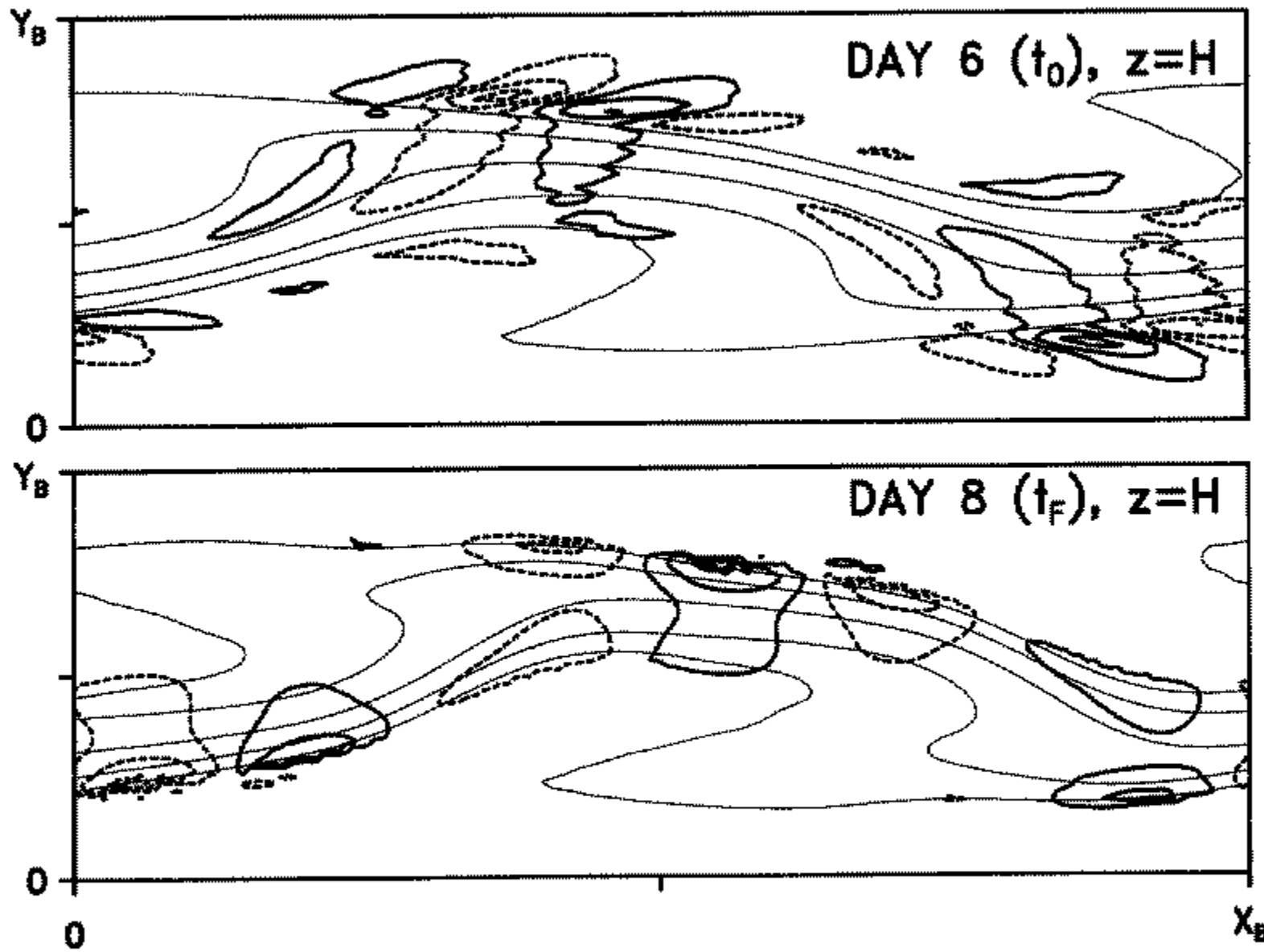


Figure 9. The optimal perturbation for a two-day interval from initial time $t_0 = 6$ d, using the long-wave basic state. Contours of potential temperature for the perturbation (thick lines) and basic state (thin lines) at $t = t_0$ (upper panel) and final time t_f (lower panel) are shown as in Fig. 3.

Thus, we repeat the calculation of section 4, but increase the wavelength of the parent wave by a factor of 4, setting $x_B = 16$. The most unstable mode at this wavelength grows through both barotropic and baroclinic processes, and at less than half the rate of the synoptic-scale mode of section 4 (HW). Because of its smaller growth rate, the mode is normalized to $\max(\bar{v}) = 3.4 \text{ m s}^{-1}$ at day 0, and we seek the most rapidly growing perturbation over the interval between $t_0 = 6$ d and $t_f = 8$ d.

The energy-optimal perturbation and basic state are shown in Fig. 9 for $t_0 = 6$ d and $t_f = 8$ d. (Fields are shown only at $z = H$ for economy of presentation.) The perturbation has a more obvious up-scale development than was the case for the synoptic-scale parent wave. The initial horizontal structure is qualitatively similar to that of the optimal perturbation to the synoptic-scale wave except that it lacks a significant zonal mean. In contrast to the synoptic-scale parent wave, however, the dominant wavelength of the perturbations always remains small compared to that of the planetary-scale parent wave, varying from $x_B/4$ at $t = t_0$ to $x_B/3$ at $t = t_f$. The energy-optimal perturbation therefore represents a secondary instability of smaller scale on the parent wave, unlike the optimal for the synoptic-scale basic state.

Consistent with the increase of baroclinity as the parent wave grows and produces frontogenesis, the amplification of 6.1 is larger than the optimal amplification for the unperturbed jet (see Fig. 6(a) for $t_0 = 0$).

6. OTHER NORMS

It is uncertain which norm, if any, is most appropriate to understanding the development of disturbances in baroclinic waves. Thus, this section describes the properties of the most rapidly growing perturbations in two additional norms, enstrophy and stream function variance. The basic state for both calculations is the synoptic-scale HW baroclinic wave and, as in section 4, we will concentrate on the case $t_0 = 4$ d and $t_f - t_0 = 2$ d.

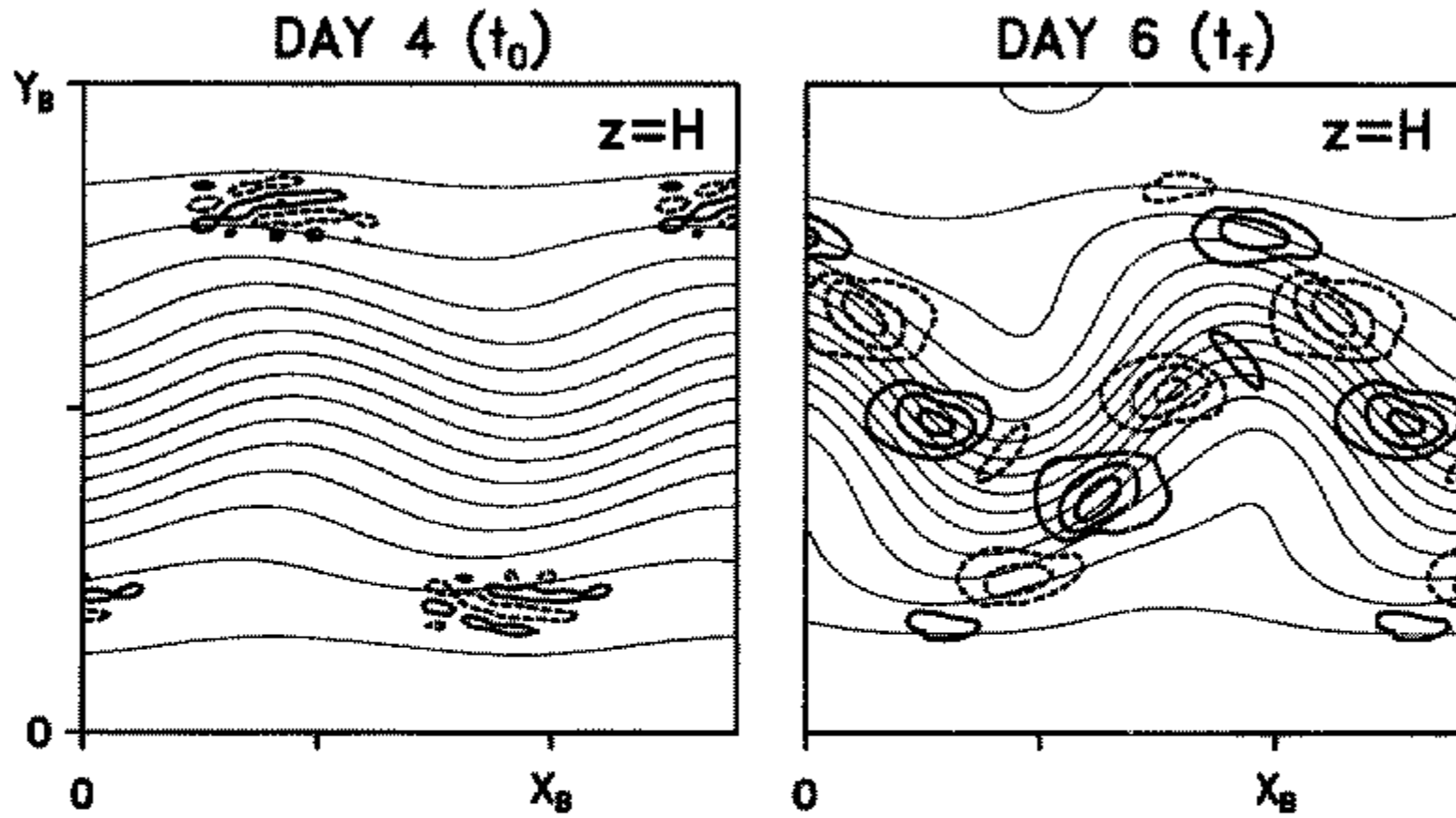


Figure 10. The optimal perturbation in the stream function variance norm for a two-day interval from initial time $t_0 = 4$ d. Geostrophic stream function for the perturbation (thick lines, negative values dashed) and basic state (thin lines) at the upper lid $z = H$ is shown for $t = t_0$ (left panels) and final time t_f (right panels). Other contouring conventions are as in Fig. 2.

The optimal perturbation for the enstrophy norm is similar to the energy optimal in its initial structure, and closely resembles the energy optimal in its evolved structure. The perturbation at initial time differs from the energy optimal principally in that its zonal mean is relatively large. At $t = t_f$, the perturbation again, to a first approximation, amounts to a phase shift of the parent wave. Not surprisingly, the two perturbations are also similar in amplification in either norm; using the energy norm, the enstrophy optimal has amplification $\nu = 4.2$, close to the maximum possible of 5.

The most rapidly growing perturbation in the stream function variance norm, in contrast, differs markedly from the energy optimal. It has amplification $\nu = 15$ in stream function variance, but this is reduced to 2.1 if the energy norm is used. The perturbation stream function at initial and final times is shown in Fig. 10, which should be compared with Fig. 3 for the energy optimal. At $t = t_0$, the stream function variance optimal consists of elongated features in ϕ' that are aligned almost zonally, have a meridional wavelength of less than 500 km, and are localized at the lid on the north (south) edges of the basic-state ridge (trough). By $t = t_f$, the perturbation has evolved into a wave train concentrated along the upper fronts and having a wavelength somewhat less than 2000 km. In Fig. 10, ϕ' is shown only at $z = H$, as surface amplitude is $1/6$ of that at the lid throughout the optimization period.

Thus, unlike the energy optimal, the stream function variance optimal has scale smaller than the parent wave, and its evolution is characterized by a significant increase in scale. Perhaps more important, however, the development of this perturbation introduces qualitatively new structure within the parent wave, where the energy and enstrophy optimals do not.

The evolution of the perturbation, shown in Fig. 11 in terms of θ' , proceeds in two phases (as did the energy optimal; Fig. 3). In the first phase, the initially elongated strips of θ' are compressed by the basic-state flow (Fig. 11, days 4–4.8). There follows a period in which the perturbation propagates as a wave along the upper fronts. The phase speed and group velocity are downstream relative to the parent wave, so that the perturbation propagates from the ridge of the parent wave into and through the base of the downstream trough, moving along the cyclonic shear side of jet. (Because of the symmetry, (5), a companion wave perturbation exists in the south-westerly flow as well.)

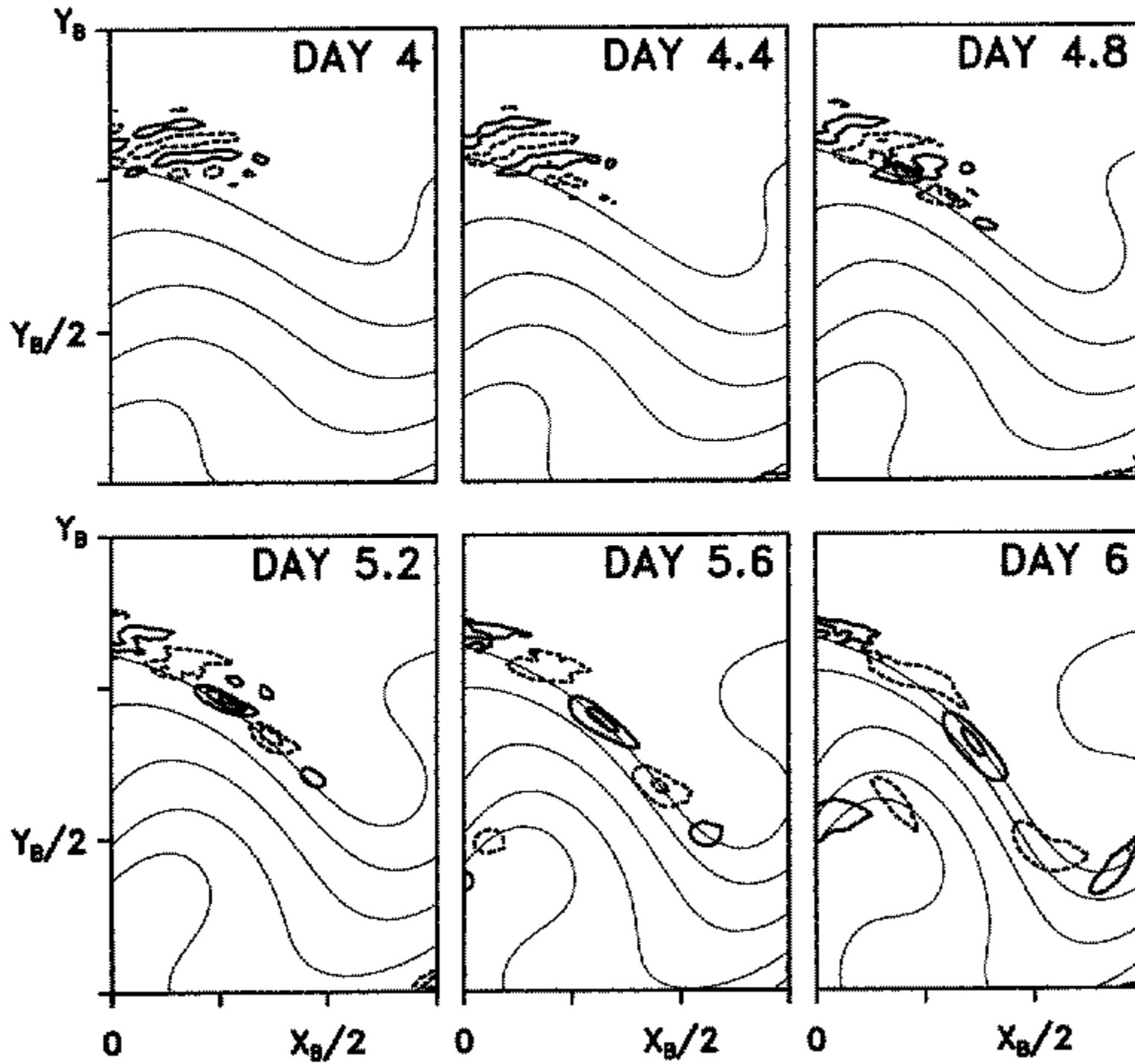


Figure 11. Time evolution of the stream function variance optimal of Fig. 10. Shown are perturbation potential temperature (thick lines; the contour interval is $1/2$ the maximum at $t = 4$ d) and basic-state potential temperature (thin lines). As in Fig. 5, the domain shown comprises only $3/4$ of a wavelength of the parent wave and only the northern $3/4$ of the channel width, and moves at the phase speed of the parent wave (12 m s^{-1}).

Figure 12 displays the evolution of the full (basic state plus perturbation) relative vorticity and ϕ at the lid. The initial perturbation in this simulation has finite amplitude with $\max \theta' = 0.9 \text{ K}$ at $z = H$ and, in order to demonstrate that the two wave trains required by (5) are dynamically independent, the initial θ' at $z = 0, H$ is set to zero for $y < y_B/2$. Maximum values of the vorticity decay during the first 12–18 hours of development (not shown), reflecting the rapid increase in scale of the disturbance. By day 5.2 (the first time shown) the wave train is established and each trough in the disturbance is marked by a vorticity maximum. These vorticity maxima, which persist even after final time for the optimization, then propagate through the parent wave and weaken in the confluent flow downstream of the parent trough.

Similar propagation is a hallmark of such synoptically familiar, upper-level features as short waves (Sanders 1988; Lefevre and Nielsen-Gammon 1995) and jet streaks (Palmén and Newton 1969); to our knowledge, this is the first idealized simulation to exhibit such behaviour. The 2000 km wavelength of the evolved perturbation is also typical of observed disturbances (Sanders 1988). Notable differences from observations are the weak penetration of the disturbances into the mid-troposphere and a lack of attendant surface cyclogenesis. Such weak penetration, however, may be alleviated in more sophisticated models that capture the lowering of the tropopause along upper-level fronts.

Finally, we note that the stream function variance optimal is poorly resolved by the numerical calculation. With doubled resolution, the optimal amplification increases to 25. The initial perturbation has smaller scale, though it remains localized in the same region and elongated in the same (almost zonal) direction, and its evolved structure is qualitatively similar to that found at lower resolution.

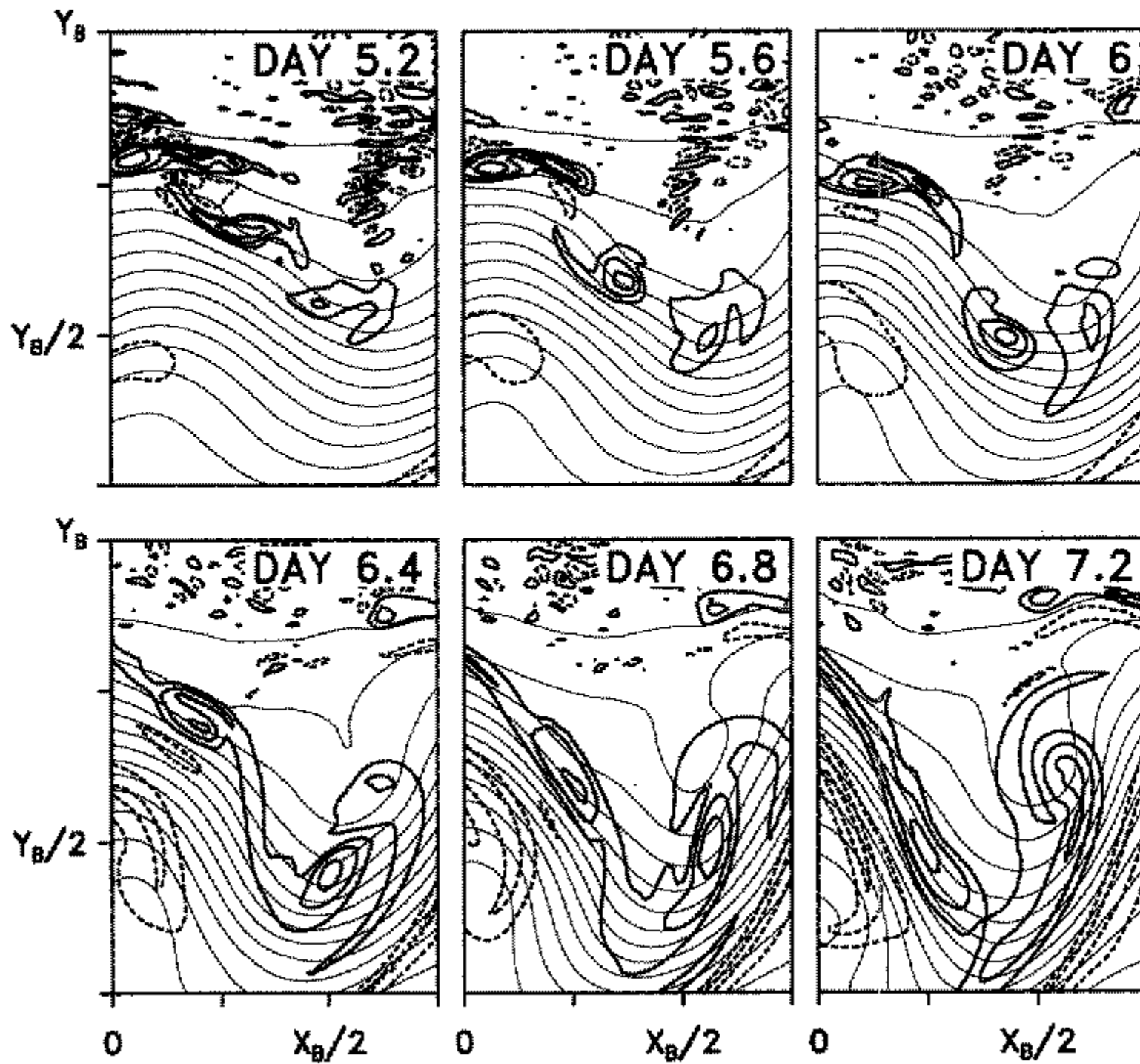


Figure 12. As Fig. 11, but using a finite-amplitude perturbation and showing the evolution of the full (basic-state plus perturbation) relative vertical vorticity (thick lines) and geostrophic stream function (ϕ , thin lines). Contour intervals are $0.6f$ for relative vorticity and $200 \text{ m}^2 \text{ s}^{-2}$ for ϕ ; the domain moves at 16 m s^{-1} in order to track the disturbance.

7. DISCUSSION

(a) Mechanisms for perturbation growth

The perturbation structure, described in sections 4–6, is generally such that the basic-state deformation tends to compress the perturbations in a horizontal plane, and ϕ' tilts with height against the basic-state vertical shear. The relation between the perturbations and the basic-state deformation can be seen more clearly in Fig. 13(a), which shows θ' at $t = 4 \text{ d}$ and $z = H$ for the stream function variance optimal on the HW basic-state wave, along with the local axis of basic-state dilatation scaled by the magnitude of the deformation. Particularly where $|\theta'|$ is largest, the perturbations are elongated in a direction subtending an angle of more than $\pi/4$ with the dilatation axis. Barotropic conversions dominate the growth of total energy, consistent with this structure and the fact that the perturbation has a surface amplitude one sixth of that at $z = H$.

The energy-optimal perturbations, with θ' maximized in roughly the same area and elongated in roughly the same direction, have a similar relation to the upper-level flow. It differs from the stream function variance optimal, however, in having larger scale, significant amplitude at the surface, and energetics that are dominated by baroclinic conversions.

In certain respects then, the perturbation development resembles that predicted by simplified models in which appropriately structured perturbations grow in basic states of uniform shear or pure deformation (for example Farrell 1989a and 1989b). Other aspects of the development, particularly the tendency for the perturbations to concentrate where $|\nabla\theta|$ is large, are also reminiscent of a wave packet propagating through a spatially varying flow as discussed in Buizza and Palmer (1995; section 2(c)).

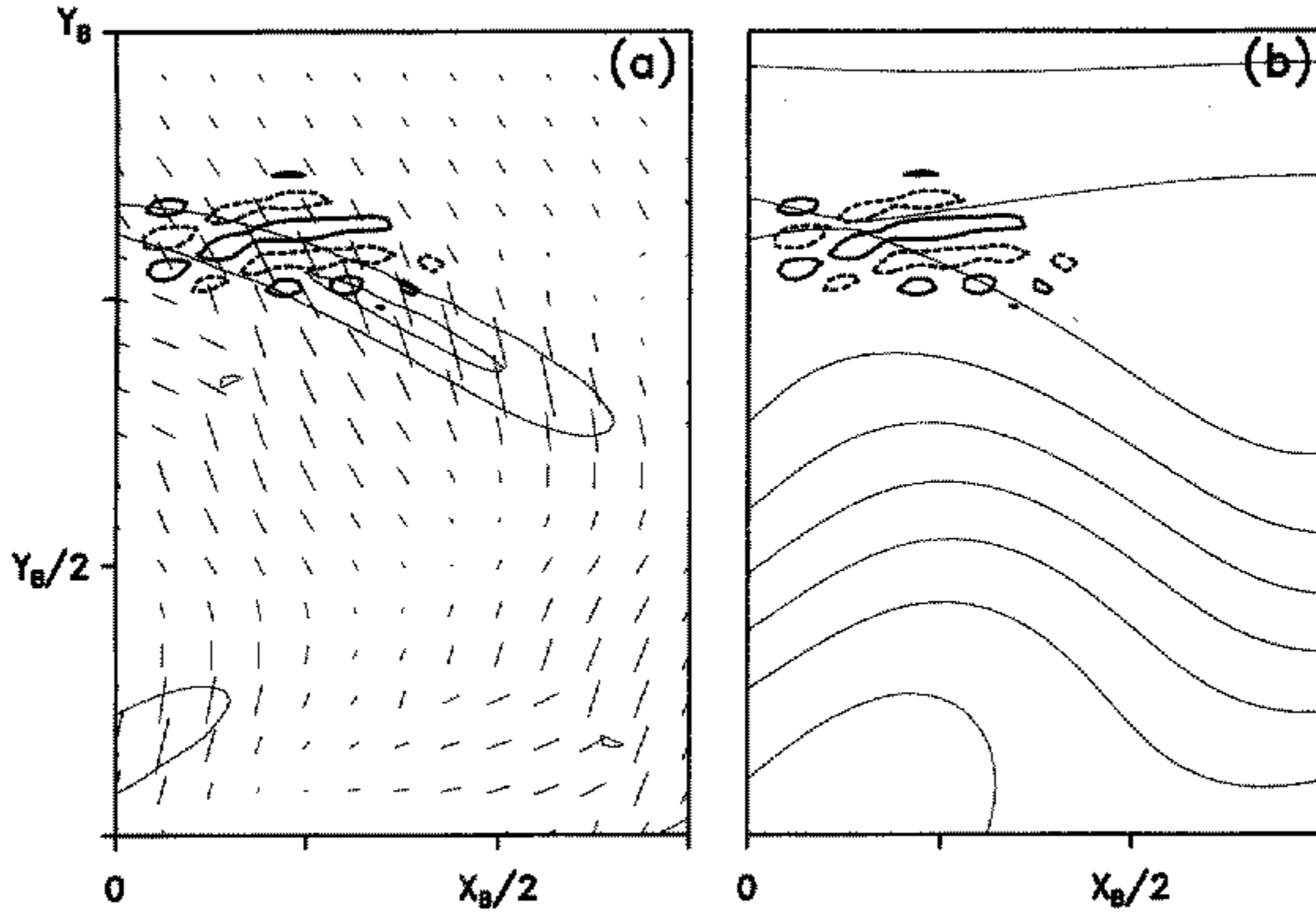


Figure 13. For the 2-day stream function variance optimal on the Hoskins and West (1979, HW in text) parent wave, the relation of perturbation potential temperature (θ') to: (a) the local axis of dilatation for the basic-state flow (thin line segments, scaled by magnitude of deformation) and the magnitude of basic-state deformation (thin contours, shown at 1/2 and 9/10 the maximum value of $2.7 \times 10^{-5} \text{ s}^{-1}$) and (b) basic-state streamlines (thin lines, contour interval $2 \times 10^6 \text{ m}^2 \text{ s}^{-1}$) in the frame of reference moving with the parent wave's phase speed (12 m s^{-1}). All fields are shown at the upper lid ($z = H$) and at initial time $t_0 = 4 \text{ d}$. Contours of θ' (thick lines) are plotted at 1/2 the maximum of θ' .

Neither of these views, however, fully explains the development of the energy- and enstrophy-optimal perturbations. First, neither is consistent with the fact that these perturbations have scale comparable with the basic-state variations. Moreover, neither view suggests that the perturbations at final time should, to a first approximation, amount to a phase shift of the parent wave.

In a flow with finite-amplitude waves, an additional mechanism exists for perturbation growth (Snyder 1998). Propagation and evolution of nonlinear waves generally depends on properties of the propagation medium as well as the waves' amplitude and structure. Initial perturbations modifying the medium, or changing the amplitude and structure of the basic-state wave, will then lead to growth of errors in the phase of the basic-state wave. (More generally, errors in the amplitude or structure of the basic-state wave may also grow.) While this mechanism cannot produce 'new' structure that is qualitatively different from the parent wave, it is consistent with both the scale and final structure of the optimal perturbations on the HW wave.

For our purposes, a simple example suffices to illustrate the essentials of the mechanism. Let the basic state consist of a finite-amplitude wave of the form

$$\bar{\psi} \sim \psi_0 \text{Re}[e^{ik(x-\bar{c}t)}] = \exp(k\bar{c}_i t) \cos k(x - \bar{c}_r t),$$

superposed on a time-independent medium. Suppose now that we perturb the medium in such a way that the modified wave, which we will now denote by ψ , has phase speed $c = \bar{c} + c'$. Perturbations then evolve as

$$\psi' = \psi - \bar{\psi} \sim kt\psi_0 \exp(k\bar{c}_i t) \{c'_i \cos k(x - \bar{c}_r t) + c'_r \sin k(x - \bar{c}_r t)\} + O(c'^2/\bar{c}^2). \quad (6)$$

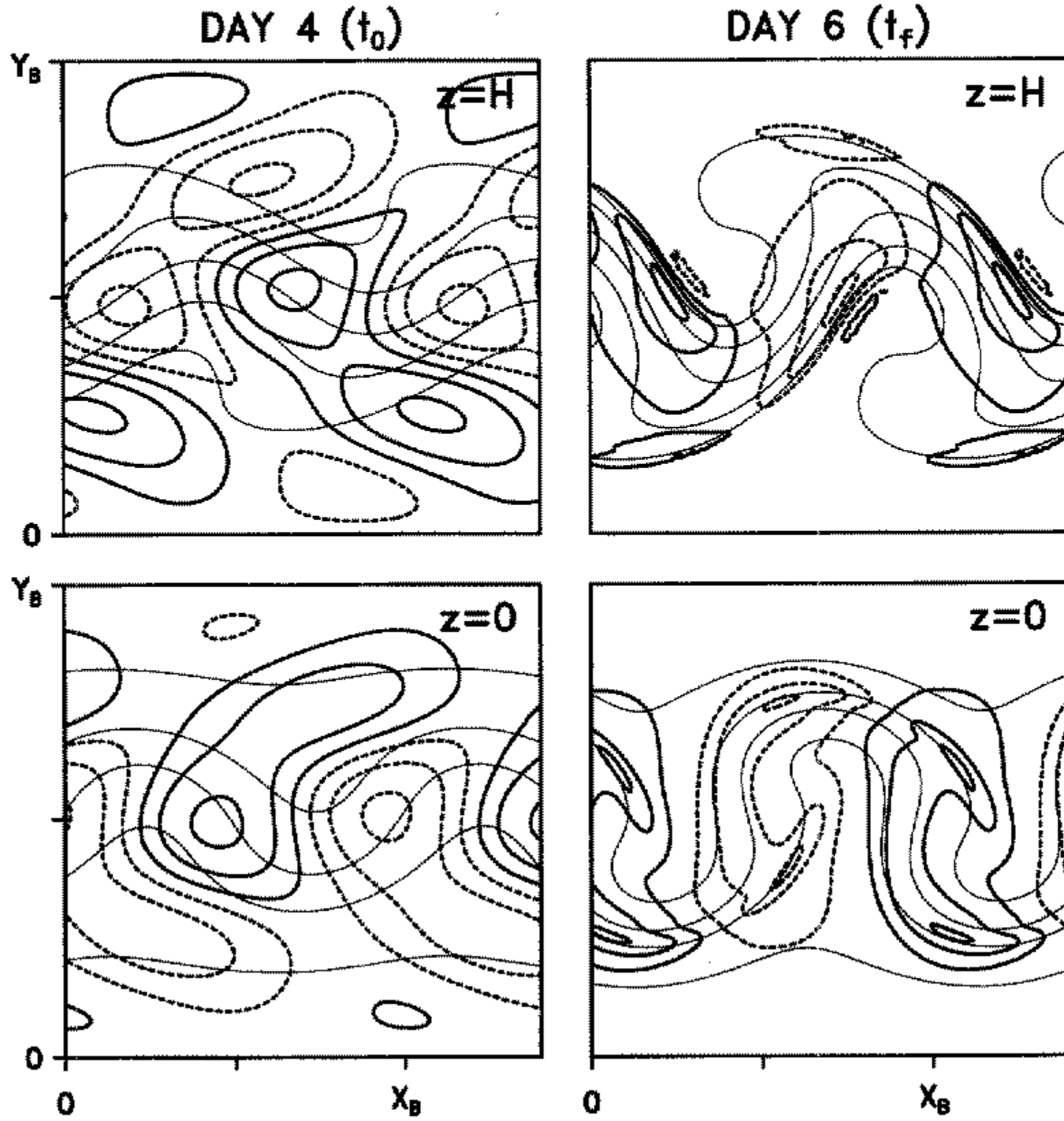


Figure 14. As Fig. 3, but with the perturbation truncated to $N = 2$ and $M(0) = 7$ (see (3)) at initial time t_0 , and increasing the contour levels by a factor of 12 at final time t_f .

Thus, small perturbations in this simple example grow as t multiplied by time dependence inherited from the basic-state wave, and have a phase shift relative to the basic state that depends on the relative modifications (c'_i/c'_r) of growth and propagation of the basic state. Note also that this mechanism requires a finite-amplitude parent wave, since the perturbation growth scales as the initial amplitude ψ_0 of the parent wave.

The prediction of (6) can be compared with the calculated optimal amplification in energy. Figure 6(b) shows the function $v(t) = \alpha t a(t)$, where $a(t)$ is the amplitude of the parent wave (replacing the exponential growth in (6)) and α is chosen so that $v(t)$ reproduces the optimal amplification for a time interval of 1 d beginning at $t_0 = 4$ d. The agreement with the calculated optimal amplification indicates that (6) is a reasonable model for the growth of the energy optimal.

For perturbations that grow as phase errors, we also expect that only scales comparable with, or larger than, that of the basic-state wave are crucial to growth. Consistent with this, wavenumbers $n = 0, 1, 2$ dominate the spectral expansion (3) of the energy optimal at both initial and final times. Moreover, truncating the initial conditions at $N = 2$ and $M(0) = 7$ in (3) reduces the amplification by just 6%, to 4.7, and alters the structure at $t = t_f$ almost imperceptibly, as can be seen by comparing Fig. 14 and Fig. 3. Even restricting the initial perturbation to have $N = 0$ and $M(0) = 5$ results in an amplification of 3.5 and qualitatively similar structure at $t = t_f$ (not shown).

Beyond day 4, the parent wave continues to grow and smaller scales become increasingly evident in the initial structure of the optimal perturbation (Fig. 7). Truncating the

initial conditions as above ($N = 2$ and $M(0) = 7$ in (3)) shows that this small-scale structure is relatively more important to the energy growth of the perturbation, but is still not crucial. When $t_0 = 6$ d and $t_f - t_0 = 2$ d, for example, truncated initial conditions decrease the amplification by 25%.

Thus, perturbations of synoptic-scale provide for much of the optimal amplification in either energy or enstrophy, by modifying the parent wave and the jet on which it propagates, and thereby engendering errors in the phase and amplitude of the parent wave. A more qualitative accounting of contributions by various mechanisms is probably impractical, given that different mechanisms can only be clearly distinguished in idealized examples.

(b) *Stabilizing influences*

The structure of the energy optimal for the synoptic-scale parent wave is surprising, since one might expect that the fronts, because of their concentrated baroclinity and horizontal shear, would support the most rapidly growing disturbances. Indeed, Joly (1995) shows that for steady straight fronts, the optimal amplification (in energy and over 2 days) is roughly 6 for fronts with maximum $\bar{\theta}_x$ of $1-2 \times 10^{-5} \text{ K m}^{-1}$, and varies little with along-front wavenumber.* The fronts within the synoptic-scale parent wave have maximum $\bar{\theta}_x$ of $1.6 \times 10^{-5} \text{ K m}^{-1}$ at day 4, increasing by factors of 2.2 and 5.6 at days 6 and 8, respectively. Assuming the amplification to scale approximately as $\bar{\theta}_x$, the results for the steady straight front suggest that frontal waves should have 2-day amplifications as large as 12 at day 6, and 30 at day 8. The actual optimal amplifications in energy are much smaller (5 between days 4 and 6, and 9 between days 6 and 8; see Fig. 6(a)) and the optimal perturbation is not a frontal wave. What then accounts for the weaker than expected instability of the fronts within the synoptic-scale parent wave?

The potential stabilizing influence of frontogenesis forced by geostrophic deformation has been demonstrated by Bishop and Thorpe (1994). Applying their conclusions to our calculations, however, is problematic: our calculations allow more general perturbations, and the optimal perturbations are generally configured to amplify, rather than decay, through interaction with the basic-state deformation. The stream function variance optimal is the most dramatic example of this, as shown in Fig. 13. Moreover, large portions of any front are under the influence of geostrophic diffluence and frontolysis, and the arguments of Bishop and Thorpe would suggest that perturbation growth should be enhanced in those regions.

But, note also that θ' tends to be concentrated where the basic-state flow relative to the parent wave is weak, rather than in the location of maximum deformation (Fig. 13(b)). Similar behaviour holds for the other basic states, and is also evident in the results of Moore and Farrell (1993). For shorter optimization intervals, the initial amplitude of the optimal shifts toward the maximum deformation (compare Fig. 3 with Fig. 8), while for longer intervals the optimal elongates into ribbons that lie along streamlines that pass near stagnation points in the flow relative to the parent wave (Fig. 7, right panel). These behaviours together suggest that the movement of the perturbation through the spatially varying basic state is a stabilizing influence, where movement may be produced by both advection by the basic state and wave-like propagation. The fastest growing perturbations seek to minimize this influence while retaining structure that is favourable (via several mechanisms) to growth.

* Joly assumes semi-geostrophy, but his results for the dependence of amplification on the basic-state baroclinity may be compared with ours (which assume quasi-geostrophy) by examining the basic state in geostrophic coordinates, where semi-geostrophic and quasi-geostrophic dynamics are equivalent. Thus, his maximum $\bar{\theta}_x$ should be divided by the Jacobian of the transformation from geostrophic to physical coordinates (see his Tables 2 and 5).

(c) *The assumption of uniform interior PV*

Equations (1a) and (2a) assume that both the basic state and perturbation have uniform interior PV. This assumption is not unreasonable for the basic state, as PV anomalies in the interior of the troposphere are of secondary importance in observed synoptic-scale cyclogenesis (Davis 1992).

The issue is less clear-cut for the perturbations. Current observations are insufficient to detect PV anomalies, which are likely to be of small amplitude and sub synoptic-scale, that might accompany perturbations within synoptic-scale cyclones.

One can argue (Joly 1995) that significant interior PV perturbations are inherently unlikely. Because interior PV in the parent wave is nearly uniform and generation of PV by diabatic process is relatively weak, interior PV perturbations will evolve to a first approximation according to advection by the basic-state wave. This advection, however, will tend to shear PV perturbations to small, and dynamically passive, scales. (Similar information would also be implicit in a calculation of the optimal perturbation using the covariance matrix \mathbf{C} for the initial perturbations to define the initial norm, $\mathbf{S}_0 = \mathbf{C}^{-1}$.) While such an argument has merit, we lack quantitative information on just how unlikely interior anomalies might be, and it is probably prudent to consider how those anomalies would modify our results.

Clearly, the structure of the optimal perturbation would change, at least in detail, if interior PV perturbations were allowed. For example, the perturbations that grow most rapidly in baroclinic flows are typically highly tilted in the mid- and lower troposphere (see, among many others: Farrell 1989a; Buizza *et al.* 1993; Mukogawa and Ikeda 1994) and require interior PV anomalies. Ehrendorfer and Errico (1995) found precisely this vertical structure in the optimal perturbation to an observed rapidly deepening cyclone, and we expect the same structure would appear in our results if interior PV were allowed.

Interior PV perturbations will also increase the optimal amplification—since the restriction to uniform interior PV is an additional constraint on the perturbation, the optimal amplification must be at least as large in a model without this restriction. As noted (section 4(b)), the amplifications found here appear to be smaller than those of Buizza *et al.* (1993) and Ehrendorfer and Errico (1995), although direct comparison is problematic.

It also seems likely that allowing non-uniform interior PV could change the scale of the optimal perturbations, at least at initial time. Energy-optimal perturbations (with non-uniform PV) for observed flows exhibit a marked increase in scale as they evolve, with their energy initially concentrated at spherical wavenumbers greater than 20 at t_0 , and between 10 and 15 at the end of the 2-day optimization period (Hartmann *et al.* 1995). In contrast, the energy-optimal perturbations with uniform PV have energy concentrated at the scale of the parent wave (roughly equivalent to spherical wavenumber 10) at both initial and final times.

The key question, of course, is whether interior PV anomalies would provide a path to qualitatively different behaviours than found here. Answers to this question are speculative at this point, but note that Ehrendorfer and Errico's (1995) results also show that the optimal perturbation at the final time represents a phase shift and deepening of the parent wave.

8. CONCLUDING REMARKS

Calculation of the most rapidly amplifying perturbation of a finite-amplitude baroclinic wave reveals that disturbances within baroclinic waves can grow rapidly, both in absolute terms and relative to the amplification of the parent wave.

The amplification and structure of the optimal perturbation depend on the norm chosen to measure growth. Using total energy as norm, that perturbation initially has largest

amplitude at the edges of the jet, and then rapidly evolves toward a final structure that corresponds to a phase shift and slight change of shape of the original wave. The optimal perturbation for the enstrophy norm closely resembles the energy optimal. For both norms, the optimal perturbation has scale comparable to or greater than that of the parent baroclinic wave throughout the 2-day interval of optimization. In contrast, the disturbance that most rapidly amplifies stream function variance is concentrated initially at scales of less than 500 km and at upper levels. It evolves into a wave train along the upper fronts with a wavelength of 2000 km. As the initial time t_0 for the optimization increases and the basic-state wave grows, there is some tendency, regardless of the norm, for the optimal initial perturbation to elongate along streamlines passing near stagnation points in the (parent) wave-relative flow.

The choice of norm also influences the mechanism by which the optimal perturbation grows. For the stream function variance norm, the development of the optimal perturbation resembles familiar finite-time generalizations of shear instabilities in simple flows (Farrell 1989a, b; Buizza and Palmer 1995). The perturbation is initially elongated normal to the dilation axis of the basic-state flow; advection by the basic state then compresses the perturbation, producing both growth and an increase of scale in the perturbation. The optimal perturbation for the energy and enstrophy norms, however, grow at least in part through the mechanism described by Snyder (1998). In this case, the initial perturbation modifies the jet upon which the parent wave propagates, and the amplitude and structure of the parent wave. These modifications then lead to changes in growth and propagation of the parent wave. This view is applicable once the parent wave has achieved significant amplitude, and explains the fact that the evolved perturbations amount to a phase shift of the parent wave.

Finally, maximal amplifications in energy are significantly less than would be expected from calculations for steady, straight fronts with horizontal temperature gradients comparable to local values in the parent wave. Although the stabilizing effects of horizontal confluence and frontogenesis (Bishop and Thorpe 1994) may play a role, circumstantial evidence presented here indicates that the movement of perturbations along the front, combined with inherent temporal and along-front variations of the basic state, is crucial in stabilizing the fronts. We speculate that disturbances will grow on the fronts only when the dynamical time-scale for growth is short relative to the time-scale for variations of the basic-state flow as seen by a moving perturbation (essentially, the advective time-scale for the basic state).

Our results also provide insight into when and how disturbances develop within baroclinic waves. Perturbing with the stream function variance optimal at finite amplitude produces a wave train along the upper front that, over a 48 h period centred on t_f , moves into and through the trough of the parent wave. The wave train has wavelength of roughly 2000 km, and its troughs are marked by maxima in vorticity at upper levels. Such behaviour is similar to that of observed short waves (Sanders 1988; Lefevre and Nielsen-Gammon 1995) and jet streaks (Palmén and Newton 1969) and has not yet been found in idealized simulations of baroclinic waves.

More generally, the north-westerly flow downstream of the parent wave's ridge is a favoured location for the development of optimal perturbations.* This property holds for the synoptic-scale basic-state wave for all the norms tested here, and also for the energy optimal on the planetary-scale wave. Synoptic experience also identifies north-westerly

* The HW baroclinic wave, and the optimal perturbations that develop on it, have the symmetry of (5). Strong upper-level fronts in observed baroclinic waves, however, typically lie only in the north-westerly flow. Basic-state waves exhibiting this asymmetry, such as that which develops on a jet with superposed cyclonic shear (section 5), support optimal perturbations that have largest amplitude in the north-westerly flow.

flow downstream of a synoptic-scale ridge as a preferred location for the intensification of upper-level disturbances that precede surface cyclogenesis (Sanders 1988, Lackmann *et al.* 1997).

Our calculations involve a number of simplifying assumptions, such as uniform interior PV and adiabatic and quasi-geostrophic dynamics. The effects of moisture should provide the most important direct modifications of the perturbation dynamics, and can be expected to enhance the amplification and reduce the scale of the optimal perturbation. The simplifying assumptions (particularly that of adiabatic and quasi-geostrophic dynamics) also have the important but indirect effect of altering the structure and evolution of the basic-state wave. For example, observed baroclinic waves are often prone to the development of secondary disturbances in the mature and decaying stages of their life cycles (e.g. Ralph 1996); we have not considered this regime, because of difficulties in reproducing the structure of mature baroclinic waves with a quasi-geostrophic model.

ACKNOWLEDGEMENTS

We thank B. Hoskins and G. Hakim for helpful suggestions. This work began during an enjoyable visit by CS to the Centre National de Recherches Météorologiques (CNRM) in Toulouse. The visit was supported by CNRM and by the National Center for Atmospheric Research. F. Lalaurette and B. Pouponneau provided able and cheerful assistance with local computing.

REFERENCES

- Blier, W. and Wakimoto, R. M. 1995 Observations of the early evolution of an explosive oceanic cyclone during ERICA IOP 5. Part I: Synoptic overview and mesoscale frontal structure. *Mon. Weather Rev.*, **123**, 1288–1310
- Bishop, C. H. and Thorpe, A. J. 1994 Frontal wave stability during moist deformation frontogenesis. Part I: Linear wave dynamics. *J. Atmos. Sci.*, **51**, 852–873
- Browning, K. A. and Roberts, N. M. 1994 Structure of a frontal cyclone. *Q. J. R. Meteorol. Soc.*, **120**, 1535–1557
- Buizza, R. and Palmer, T. N. 1995 The singular-vector structure of the atmospheric general circulation. *J. Atmos. Sci.*, **52**, 1434–1456
- Buizza, R., Tribbia, J., Molteni, F. and Palmer, T. 1993 Computation of optimal unstable structures for a numerical weather prediction model. *Tellus*, **45A**, 388–407
- Davies, H. C., Schär, C. and Wernli, H. 1991 The palette of fronts and cyclones within a baroclinic wave-development. *J. Atmos. Sci.*, **48**, 1666–1689
- Davis, C. A. 1992 A potential vorticity diagnosis of the importance of initial structure and condensational heating in observed extratropical cyclogenesis. *Mon. Weather Rev.*, **120**, 2409–2428
- Ehrendorfer, M. and Errico, R. M. 1995 Mesoscale predictability and the spectrum of optimal perturbations. *J. Atmos. Sci.*, **52**, 3475–3500
- Ehrendorfer, M. and Tribbia, J. J. 1996 Optimal prediction of forecast error covariances through singular vectors. *J. Atmos. Sci.*, **53**, 286–313
- Farrell, B. F. 1989a Optimal excitation of baroclinic waves. *J. Atmos. Sci.*, **46**, 1193–1206
- 1989b Transient development in confluent and diffluent flow. *J. Atmos. Sci.*, **46**, 3279–3288
- Hartmann, D. L., Buizza, R. and Palmer, T. N. 1995 Singular vectors: The effect of spatial scale on linear growth of disturbances. *J. Atmos. Sci.*, **52**, 3885–3894
- Hoskins, B. J. and West, N. V. 1979 Baroclinic waves and frontogenesis. Part II: Uniform potential vorticity jet flows—cold and warm fronts. *J. Atmos. Sci.*, **36**, 1663–1680
- Houtekamer, P. L. 1995 The construction of optimal modes. *Mon. Weather Rev.*, **123**, 2888–2898
- Houze, R. A. 1993 *Cloud dynamics*, Academic Press, San Diego, USA
- Joly, A. 1995 The stability of steady fronts and the adjoint method: Nonmodal frontal waves. *J. Atmos. Sci.*, **52**, 3082–3108

- Joly, A. and Thorpe, A. J. 1990 Frontal instability generated by tropospheric potential vorticity anomalies. *Q. J. R. Meteorol. Soc.*, **116**, 525–560
- Lacarra, J.-F. and Talagrand, O. 1988 Short-range evolution of small perturbations in a barotropic model. *Tellus*, **40A**, 81–95
- Lackmann, G. M., Keyser, D. and Bosart, L. F. 1997 A characteristic life cycle of upper-tropospheric cyclogenetic precursors during the Experiment on Rapidly Intensifying Cyclones over the Atlantic (ERICA). *Mon. Weather Rev.*, **125**, 2729–2758
- Lefevre, R. J. and Nielsen-Gammon, J. W. 1995 An objective climatology of mobile troughs. *Tellus*, **47A**, 638–655
- Lorenz, E. N. 1965 A study of the predictability of a 28-variable atmospheric model. *Tellus*, **17**, 321–333
- Malardel, S., Thorpe, A. J. and Joly, A. 1997 Consequences of the geostrophic momentum approximation on barotropic instability. *J. Atmos. Sci.*, **54**, 103–112
- McWilliams, J. C. and Gent, P. R. 1980 Intermediate models of planetary circulations in the atmosphere and ocean. *J. Atmos. Sci.*, **37**, 1657–1678
- Moore, A. M. and Farrell, B. F. 1993 Rapid perturbation growth on spatially and temporally varying oceanic flows determined using an adjoint method: Application to the Gulf Stream. *J. Phys. Oceanogr.*, **23**, 1682–1702
- Mukogawa, H. and Ikeda, T. 1994 Optimal excitation of baroclinic waves in the Eady model. *J. Meteorol. Soc. Jpn.*, **72**, 499–513
- Palmén, E. and Newton, C. W. 1969 *Atmospheric circulation systems: their structure and physical interpretation*, Academic Press, New York
- Palmer, T. N., Gelaro, R., Barkmeijer, J. and Buizza, R. 1998 Singular vectors, metrics and adaptive observations. *J. Atmos. Sci.*, **55**, in press
- Pedlosky, J. 1987 *Geophysical fluid dynamics*, Springer-Verlag, New York
- Ralph, F. M. 1996 Observations of 250-km-wavelength clear-air eddies and 750-km-wavelength mesocyclones associated with a synoptic-scale midlatitude cyclone. *Mon. Weather Rev.*, **124**, 1199–1210
- Rotunno, R. and Bao, J.-W. 1996 A case study of cyclogenesis using a model hierarchy. *Mon. Weather Rev.*, **124**, 1051–1066
- Sanders, F. 1988 Life history of mobile troughs in the upper westerlies. *Mon. Weather Rev.*, **116**, 2629–2648
- Snyder, C. 1995 Stability of steady fronts with uniform potential vorticity. *J. Atmos. Sci.*, **52**, 724–736
- 1998 Error growth in flows with finite-amplitude waves or coherent structures. *J. Atmos. Sci.*, **55**, in press
- Vukicevic, T. 1993 Possibility of skill forecast based on the finite-time dominant linear solutions for a primitive equation regional model. *J. Atmos. Sci.*, **50**, 1777–1791